

2

High-Power Fiber Lasers and Amplifiers: Fundamentals and Enabling Technologies to Enter the Upper Limits

Thomas Schreiber, Ramona Eberhardt, Jens Limpert, and Andreas Tünnermann

2.1

Introduction

It is understood that several enabling technologies have been responsible for the rapid performance scaling of fiber laser systems and their huge market success in different applications. Firstly, as for most solid state lasers, highly efficient and reliable diode lasers are one of the most essential parts for delivering pump photons. Secondly, the generation and control of light inside a fiber laser would not be possible without the use of low loss rare-earth doped optical fibers. Additionally, the application of integration technologies as well as different fiber-based optical components into alignment-free laser systems enabled the usability outside the laser laboratory.

Originally, the development of optical fibers utilized the potential of optical communication technology to allow transmission of vast amounts of data over huge distances. A major breakthrough was achieved when low loss glass fibers were manufactured for the first time by Corning in 1970 [1]. In the years that followed, these fibers replaced copper wires and almost all commercial telecommunication and network systems worldwide were built on fiber technology, thereby revolutionizing the method of information delivery and processing on a global scale. The fabrication technology allowing the production of fibers with the required properties had not been possible before the 1970s, when the chemical vapor deposition technique for producing fused silica was adapted. Previously, the large attenuation of fibers only enabled short light path transmission in instruments such as medical endoscopes or those used for illumination. Nevertheless, with the work on medical endoscopes driven by van Hell in 1954 and L. Curtiss in 1956, fibers had been made where guiding was achieved by a lower refractive index cladding surrounding a higher index core. The theoretical description of fibers as cylindrical waveguides, especially single mode fibers, was brought forward by E. Snitzer [2] in the early 1960s after he recognized the first waveguide modes found accidentally by W. Hicks. This theoretical basis together with the rapidly improving fabrication technology led to the realization of low loss single mode fibers that were applicable to information transmission.

Beside the fact that the first flash-lamp pumped fiber laser was realized in 1961 and used a neodymium (Nd)-doped crown glass as the core surrounded by an ordinary soda-lime-silicate glass, giving three inch long fiber samples [3], the telecommunication industry promoted its development by requiring an amplification scheme for intercontinental undersea transmission lines. Such amplification in a fiber has been shown by a rigid Nd-doped fiber wound around a flash lamp [4]. The replacement of flash lamps for pumping solid state laser was recognized and demonstrated in the early 1960s by the use of diode lasers, but they had no practical appearance until room temperature operation was possible in these semiconductor devices in the 1980s [5]. Diode lasers and erbium-doped fibers have been the basis of the optical amplifier now used for most long haul transmission lines, developed in 1987 [6].

Despite the success of optical fibers in telecommunication a second revolution started just after the twenty-first century began. With the availability of high power, high brightness diode lasers to pump double clad fibers doped with rare-earth elements to provide the active laser medium, the race for high power and energies from single mode fiber lasers began [7].

In the following sections the principles of high-power fiber lasers are reviewed. The design of double clad fibers that enable highest power levels are discussed in Section 2.2. Included is a review of the tailored optical properties of photonic crystal fibers, which have huge potential in future scaling efforts. Section 2.3 gives the basics required to theoretically describe the fiber lasers. This is followed by a brief discussion of additional high-power components and examples of high-power experiments in Sections 2.4 and 2.5, respectively.

2.2

High-Power Fiber Design

2.2.1

Double Clad Fiber Design

In its simplest form, a high-power laser fiber is designed as a double clad structure. The first cladding surrounds a doped core, where the core's refractive index is typically set to only guide the fundamental mode. The second cladding is the pump cladding that is formed by a multimode waveguide with a much larger area and numerical aperture. The pump light that is typically delivered by diode lasers can be coupled to the pump cladding with a high efficiency but is only weakly absorbed in this case. However, the small signal absorption along the fiber is not described by an exponential decay (Beers law) [8] due to the existence of modes having a quite low spatial overlap with the doped core and which are therefore negligibly absorbed. To avoid such modes the fibers may be coiled or the symmetry within the double clad structure can be broken. Symmetry breaking ensures an intrinsic absorption independent of bending and is typically favored. Figure 2.1 shows examples with an offset core or modified shapes.

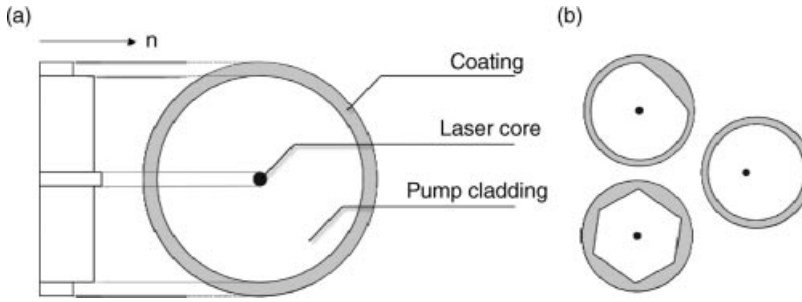


Figure 2.1 (a) Double clad fiber design and refractive index distribution; (b) symmetry breaking by geometry for a D-shaped and hexagonal pump core as well as offset-core fiber.

The core is typically doped with rare earth elements to provide the laser ions. Figure 2.2 gives an overview of some rare earth elements and their possible lasing wavelength in the visible and near-infrared region. The most prominent example is erbium, which is used to realize erbium-doped fiber amplifiers (EDFAs) for telecommunication networks [9]. Currently, the highest power levels out of a fiber laser are obtained with ytterbium (Yb^{3+} by Yb_2O_3) doped fused silica fibers, which will be focused on in the following.

The refractive index increase Δn of the fiber's core is determined by the rare earth content and also by the concentration of other co-dopants. In most cases, a linear addition rule is valid with respect to the molar composition with constant increments [10]. Figure 2.3 shows the molar index changes of rare earth and co-dopants typically used. Apart from B_2O_3 and SiF_4 all conventional rare earth and other co-dopants for silica fibers exhibit a positive value for the molar index change. Thus, high dopant concentrations generally increase the core index significantly with respect to the surrounding cladding and alter the guiding properties of the fiber. The molar refractivity change is very high for Yb_2O_3 doping, and it is therefore difficult to design a fiber core with a low index increase Δn without co-doping the core with negative index materials such as SiF_4 or B_2O_3 . Moreover, when higher concentrations are used to achieve high absorption values, the addition rule no longer holds and more complicated design rules have to be determined [11].

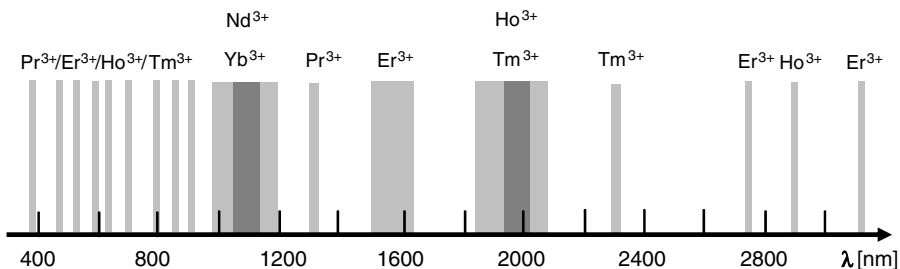


Figure 2.2 Accessible wavelengths by rare earth doping.

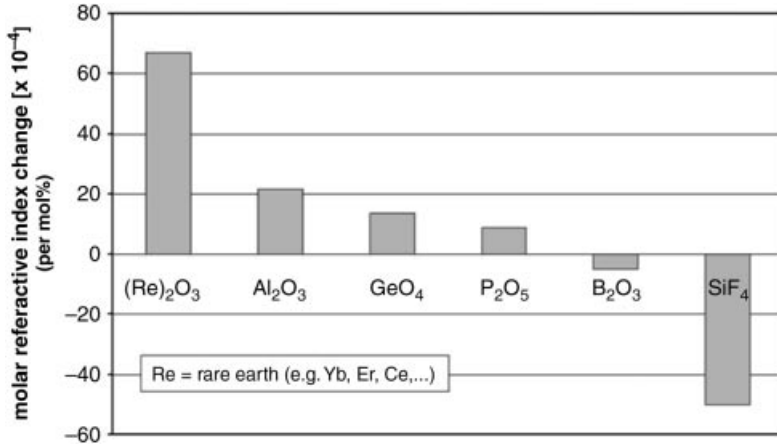


Figure 2.3 Molar refractive index changes for commonly used rare earth dopants and co-dopant materials in silica glass.

The waveguide properties of a fiber core can theoretically be described by eigenvalue analysis of the propagation equation (2.1). The equation is known as the scalar Helmholtz equation and is an approximation assuming no external sources and currents for the material properties with no transverse dependence of the dielectric function $\varepsilon(x,y,\omega) = n(\omega)^2$, weak guidance, and no favor of a polarization state. It is not applicable to all fiber designs; however, it leads to good insight into the physics [12]:

$$\left(\frac{\partial^2}{\partial x^2} + \frac{\partial^2}{\partial y^2} \right) F + \varepsilon(\omega) \frac{\omega^2}{c^2} F = \beta^2 F \quad (2.1)$$

As a result, different modes $F(x,y)$ and their propagation constants β are calculated, as can be seen schematically in Figure 2.4 for a circular core with a radius a_{eff} and the first two modes LP01 and LP11. The propagation constant β is related to the effective

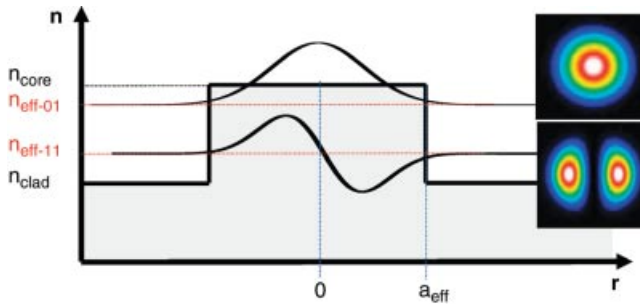


Figure 2.4 Schematic representation of the refractive index profile in a step index fiber and the resulting effective index for the first two modes shown with their typical intensity profiles $|F(x,y)|^2$.

index of the guide's mode by $\beta(\omega) = n_{\text{eff}}(\omega) \cdot \omega/c$, with a value that is smaller than the core index n_c and larger than the index of the surrounding cladding n_{clad} . For step index fibers approximations have been made and a normalized frequency parameter V as well as the parameters U and W can be defined as:

$$V = \frac{2\pi}{\lambda} a_{\text{eff}} N_A = \frac{2\pi}{\lambda} a_{\text{eff}} \sqrt{n_c^2 - n_{\text{clad}}^2} = \sqrt{U^2 + W^2} \quad (2.2)$$

where $U = \frac{2\pi}{\lambda} a_{\text{eff}} \sqrt{n_c^2 - n_{\text{eff}}^2}$ and $W = \frac{2\pi}{\lambda} a_{\text{eff}} \sqrt{n_{\text{eff}}^2 - n_{\text{clad}}^2}$

These parameters can be used to provide a unified way to describe basic guiding properties. For weakly guiding step index fibers, these values can be expressed by semi-analytical equations [13] and it has been shown that only the fundamental mode is guided, if $V < 2.405$. To achieve this, the core index has to be controlled carefully. The resulting nearly Gaussian mode has a $1/e^2$ mode field diameter (MFD) that is related to the V parameter by the Marcuse equation [14] to a good approximation within a range of $V \sim 0.8$ – 2.5 by Equation 2.3. To describe nonlinear effects, it is more convenient to use the effective area A_{eff} of the mode, with its definition in Equation 2.4 based on the actual profile field $F(x,y)$ of the mode:

$$\frac{\text{MFD}}{2a_{\text{eff}}} \sim 0.65 + \frac{1.619}{V^3} + \frac{2.879}{V^6} \quad (2.3)$$

$$A_{\text{eff}} = \frac{\left(\iint |F(x,y)|^2 dx dy \right)^2}{\iint |F(x,y)|^4 dx dy} \quad (2.4)$$

2.2.2

Large Core Design in Special Fibers

2.2.2.1 Motivation

As will be discussed below, nonlinear effects limit the achievable power out of fiber laser systems. The use of larger cores reduces nonlinear effects due to the reduction of propagating intensity along the fiber. For single-mode fibers ($V < 2.4$), the enlargement of the core requires the reduction of the core N_A according to Equation 2.2. This is practically limited for several reasons. Firstly, the characterization and knowledge and control of the refractive index before drawing the fiber is limited to 10^{-4} by measurement technology, which might be overcome by characterizing the mode quality of the drawn fiber. Secondly, lowering the refractive index might be difficult due to the required concentration level of the rare-earth ions to provide sufficient absorption. As a result, typical so-called large mode area (LMA) fibers with core diameters above $15 \mu\text{m}$ are able to guide several transversal modes.

Several techniques have been implemented to provide single-mode operation in these LMA fibers, such as modified matching [15], differential bend loss for higher-order modes (HOMs) [16, 17], resonant out-coupling of HOMs [18], mode filtering with tapers [19], confined doping [20], and gain-guiding index-anti-guiding [21].

However, the step index fiber discussed briefly in the last section is by no means the only method available to define a large single-mode core inside a fiber. By including additional refractive index structures in the fiber, one can greatly tailor additional optical parameters. One successful example of such microstructuring is the inclusion of regularly spaced air-filled holes that run along the length of the fiber. These fibers are also known as photonic crystal fibers (PCFs). Indeed, up to now the largest mode field diameter combined with the highest average power has been demonstrated using PCF [22–24]. The advantage of this type of fiber is based on the geometrical design freedom and control in addition to the doping profile used in step index fibers.

2.2.2.2 Core Design in Photonic Crystal Fibers

The geometrical parameters for standard step index fibers and PCFs, which are defined by a regular hexagonal array of air-holes, are compared in Figure 2.5 with the dimensional parameters a_{eff} as the core radius, Λ as the hole to hole center distance (pitch), and d as the hole diameter. The core of the PCF is defined by one missing air-hole in the center of the structure.

To investigate the modal properties of such PCFs, the parameters V , U , and W can be employed, if the effective indices of the actual structure are used. For PCFs, both, n_{eff} and n_{clad} and therefore V , U , and W have to be evaluated numerically. Numerous attempts have been made to improve the accuracy and speed of the computations based on different approaches like beam propagation, finite difference schemes, and different functional expansion methods [25]. For a wide range of parameters empirical relations can be used, which have been fitted to these numerical results and have been used here for solid core PCFs to simplify the design in terms of calculating the fundamental properties [26].

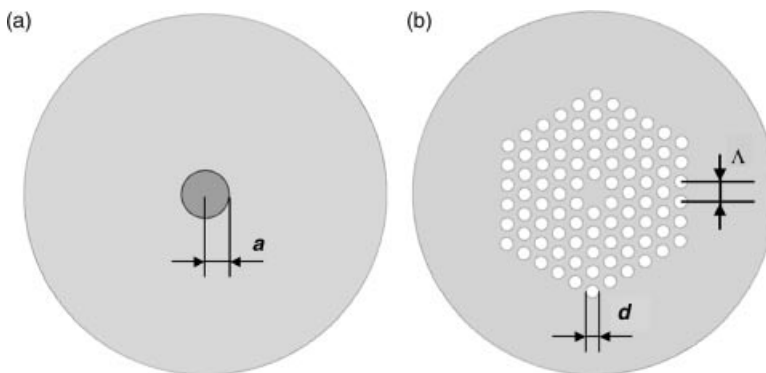


Figure 2.5 Geometrical parameters for a step index fiber (a) and a photonic crystal fiber (b); (a – core radius, d – hole diameter, Λ – pitch).

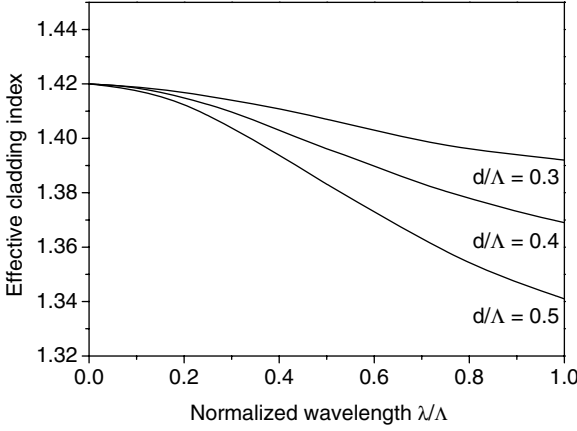


Figure 2.6 Effective cladding index of a photonic crystal fiber versus normalized wavelength λ/Λ for different relative hole sizes (d/Λ).

The parameter a_{eff} is equal to the core radius for step index fibers (SIF) and corresponds to $\Lambda/\sqrt{3}$ for PCFs with one-hole missing. With the definition of Equation 2.2 one can show that a PCF becomes single-mode for $V < 2.405$, just as for a SIF. The main difference between a SIF and PCF is that for PCF the cladding index is strongly dependent on λ/Λ (Figure 2.6), where the refractive index of the solid matrix of fused silica n_{SiO_2} (assumed constant over wavelength) is set to 1.42. In the limit of large spacing Λ or vanishing hole diameters compared to the wavelength λ , the effective cladding index reaches the core index.

Figure 2.7 shows examples of effective indices n_{eff} one obtains for the fundamental mode in typical SIFs and PCFs, where n_{eff} is plotted against the normalized

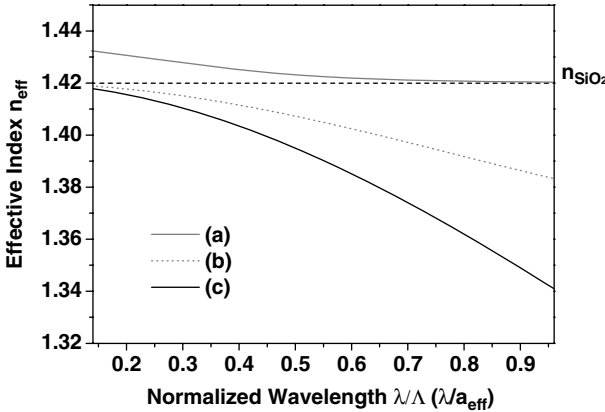


Figure 2.7 Effective index n_{eff} of the fundamental mode with respect to the normalized wavelength λ/Λ (λ/a_{eff}) for (a) a step index fiber with $2a = 6.6 \mu\text{m}$ and

$n_{\text{core-SiO}_2} = 1.2 \times 10^{-3}$, (b) single mode PCF with $\Lambda = 10 \mu\text{m}$, $d/\Lambda = 0.4$, and (c) highly nonlinear PCF with two zero dispersion wavelengths $\Lambda = 1 \mu\text{m}$, $d/\Lambda = 0.8$.

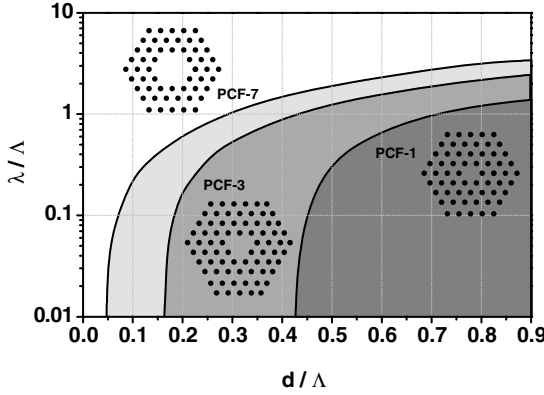


Figure 2.8 Modal characteristics of a one-, three-, and seven-hole-missing photonic crystal fiber; gray: multi-mode region.

wavelength, which is λ/a_{eff} for standard step index fibers and λ/Λ for photonic crystal fibers. For the SIF, the cladding index n_{clad} is that of fused silica and the core index n_{C} is raised to provide the necessary index step for guidance. The cladding index n_{clad} is almost constant with wavelength for step index fibers (neglected chromatic dispersion), but in the case of a PCF corresponds to the effective index of the fundamental space-filling mode of the holey cladding. The results become more interesting when plotting the single mode boundary $V = 2.405$ of the normalized wavelength over the relative hole diameter as carried out in Figure 2.8 not only for a PCF with only one hole removed to form the core (PCF-1) but also a three hole missing design (PCF-3) and a seven hole missing design (PCF-7) [27].

In PCF-1 the fiber turns from multi-mode operation into single mode operation for $d/\Lambda > 0.424$ if the normalized wavelength is large enough. For $d/\Lambda < 0.424$ this fiber becomes single mode for all wavelengths λ/Λ because the wavelength dependence of n_{clad} keeps the N_{A} low enough to stay single mode. This behavior is called endlessly single mode. It was observed in the first photonic crystal fibers and was investigated theoretically soon after that [28, 29]. Such an endlessly single mode operation is not known in SIFs and leads to the concept of scaling the core diameter of a photonic crystal fiber, since the pitch Λ , and thereby the mode field diameter, could in principle be arbitrary scaled up in the regime. The boundaries for the other designs are different – in particular the endlessly single mode condition is $d/\Lambda < 0.165$ and $d/\Lambda < 0.046$ for PCF-3 and PCF-7, respectively.

Nonetheless, the advantage of an additional control of how the light is captured within the holes remains true even for more sophisticated designs. Even though such PCFs have played a fundamental role in enabling this scaling in mode area and power/pulse energy in fiber laser systems, a strict analytical consideration shows that these fibers are actually not single-mode [30]. This is due to the finite outer cladding, so that all PCF are indeed leaky waveguides and the fundamental mode has to be discriminated to the next higher order mode of the hole structure. By proper design, it is possible to achieve *effective* single-transverse-mode operation by offering higher

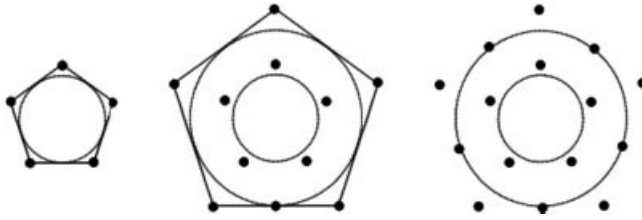


Figure 2.9 Example of non-hexagonal fiber design: building instructions for a pentagonal two-ring large pitch fiber core region.

confinement losses for HOMs compared to the fundamental mode (FM), that is, by exploiting mode discrimination. This concept was introduced by P. Russell as “modal sieve” in the context of endlessly single-mode fibers [31]. Very large mode area fibers using this effect are also known as leakage channel fibers [32]. However, this label is misleading for double clad structures and, therefore, the more general definition of large-pitch photonic crystal fiber (LPF) is preferred [33, 34]. This term makes reference to the fact that the hole-to-hole distance (pitch Λ) is at least ten-times larger than the wavelength to be guided. Novel developments aim for even higher mode discrimination by exploring lower symmetries for the arrangement of holes [35], as shown schematically in Figure 2.9. Finally, a complex analysis of the whole waveguide including the pump core and, for example, its bending has to be considered to maintain a stable output mode [36].

2.2.3

Pump Core Design

The pump core of a double clad fiber is usually defined by a low index polymer coating or a low index doped glass as the outer cladding. Depending on the index difference, numerical apertures for the pump core of up to 0.45 are possible by such methods. It is also possible to form an air-cladding region to create double-clad fibers. Such an air-cladding can be achieved by surrounding the inner cladding with a web of silica bridges (Figure 2.10). A simple calculation evaluating the effective index n_b of the fundamental mode in the silica bridge (slab waveguide with the diameter of the bridge width) to determine the numerical aperture is shown in Figure 2.10b. This simplified calculation is in excellent agreement with experiments and full calculations [37]. If the bridge width is substantially narrower than the wavelength of the guided radiation, a higher numerical aperture compared to conventional polymer or glass double clad fibers ($NA \approx 0.4$) can be achieved. This allows the diameter of the inner pump cladding to be reduced, while maintaining sufficient numerical aperture for efficient pumping. The advantage of shrinking the inner cladding is that the overlap ratio of the core to the inner cladding increases, leading to shorter absorption lengths – and thus higher thresholds for nonlinear effects. Alternatively, the large index step between the inner and outer claddings can lead to very large numerical apertures (≈ 0.8) [38]. These large numerical apertures greatly reduce the need for sophisticated coupling optics of

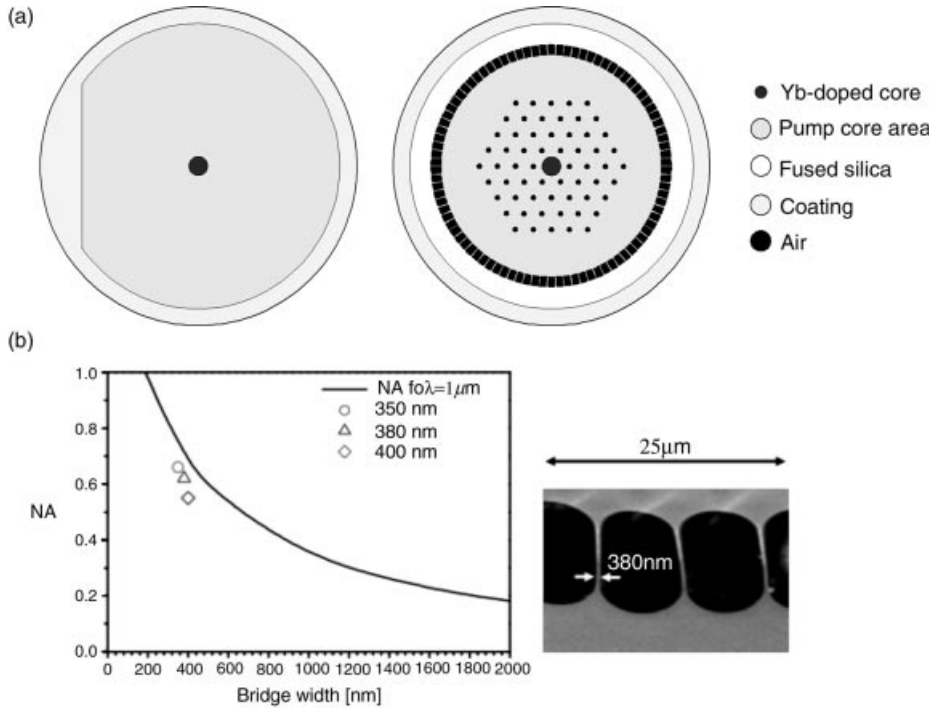


Figure 2.10 (a) Schematic comparison of a step-index double clad fiber (left) and a microstructured double clad fiber consisting of a microstructured core and an air-cladding

region (right); (b) theoretical dependence of the NA of the air-cladding on the bridge width. The measured values for different bridge width are also shown.

high-power diode laser stacks into the active fiber if the diameter of the inner cladding is not reduced. Furthermore, no radiation has direct contact with the coating material (and therefore cannot burn it), which avoids another common problem with conventional fibers. Figure 2.11 shows some realizations of air-clad photonic crystal fibers: a three-missing hole core design (Figure 2.11a), a 19-missing hole design (Figure 2.11b), and also advanced designs with different hole diameters to provide single-mode guidance (Figure 2.11c) as well as a seven-hole missing design but with a web-type air-cladding (left inset Figure 2.11d).

2.2.4

Polarization Control

Beside the innovative inclusion of the double clad design by means of air-holes and the realization of large single-mode cores by a microstructured cladding, further optical properties can be included while maintaining all other advantages and properties. For instance, polarization control is added to a waveguide by sufficient birefringence. For isotropic fibers, the modal birefringence (the difference in the

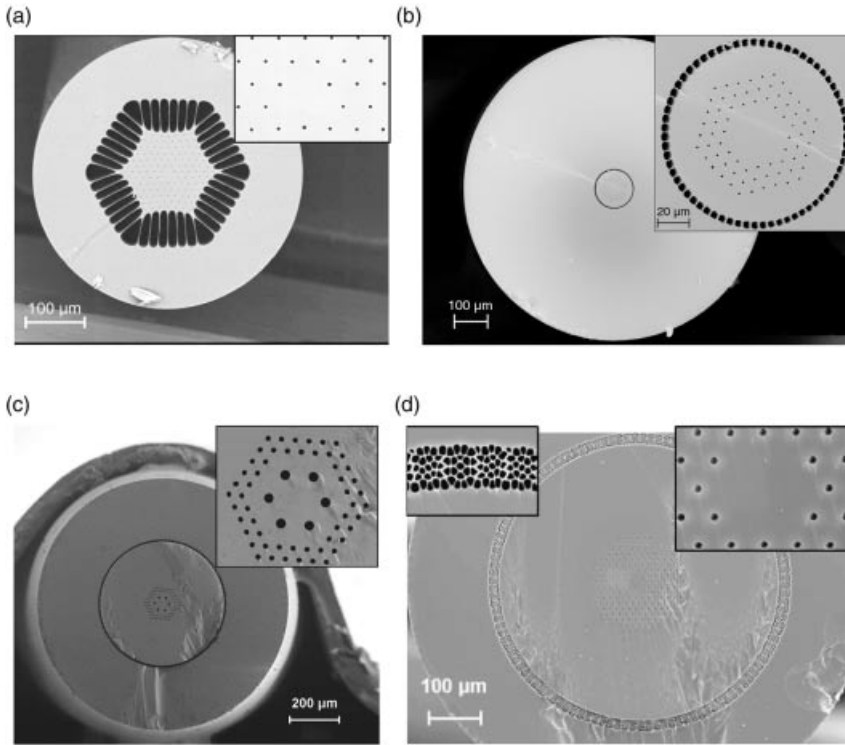


Figure 2.11 Various realizations of double clad PCFs.

effective index for both polarization states) almost vanishes and is of the order of 10^{-6} due to fabrication irregularities. Enough birefringence can be obtained by form birefringence or material anisotropy. Form birefringence can be realized, for instance, by elliptical cores in step index fibers. Despite the realization of elliptical cores in photonic crystal fibers, small variations in the symmetry of the cladding structure can also break the degeneracy of the two polarization states of the fundamental mode. Using this technique, a high birefringence can simply be obtained with different air-hole sizes in twofold symmetry surrounding the core [39]. Especially for small core PCF, a higher level of form birefringence ($B \approx 10^{-3}$) can be obtained compared to step index fibers, which can again be attributed to the higher index contrast of fused silica to the air-holes [40].

Nevertheless, the implementation of form birefringence suffers from the disadvantage that it decreases rapidly for larger cores [Noda86]. Thus, as an alternative, material anisotropy can be introduced to the fiber core. This can be achieved by external forces or by the well-known technique of stress-applying parts (SAP) inside the fiber, where the elasto-optical effect introduces anisotropy and therefore birefringence. The latter offers the advantage of an intrinsically permanent birefringence. In addition, there is the advantage of a relatively low wavelength dependence of the stress-induced birefringence [41], which results from the low dispersion of the

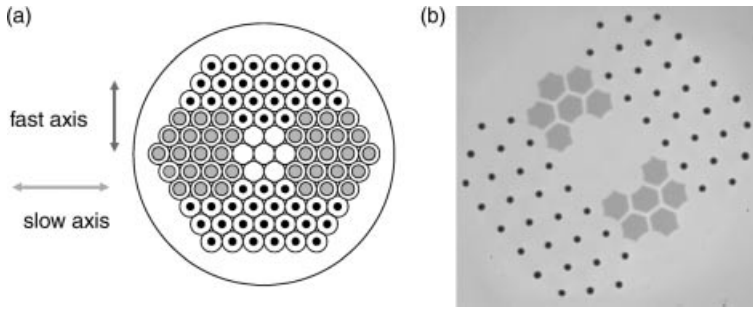


Figure 2.12 (a) Design of a polarization maintaining large mode area (seven missing holes to form the core) photonic crystal fiber consisting of index-matched stress applying elements (largely-filled circles) as part of the photonic cladding; (b) microscopic image of a realized fiber.

stress-optical coefficient. In combination with the large single-mode wavelength range of photonic crystal fibers, stress-induced birefringent fibers can provide a large highly birefringent bandwidth [42].

To achieve this, the stress applying elements, which are usually placed apart from the core, (or even the inner photonic cladding) are moved close to the core. At the same time, the guiding properties of the single-mode core should not be affected. Figure 2.12 shows the basic idea.

The stress applying elements consist of a material with a different thermal expansion coefficient α to that of the surrounding cladding material [fused silica (FS)]. Using boron-doped silica (BS) with $\alpha_{BS} = 5 \times 10^{-7} \text{ K}^{-1}$ compared to $\alpha_{FS} = 10 \times 10^{-7} \text{ K}^{-1}$, a permanent stress field can be generated when cooling the fiber below the softening temperature during the drawing process. Because the refractive index of this material is lower than that of fused silica ($\Delta n = -0.008$), a similar periodic inner cladding compared to that of the air-hole cladding can be constructed (Figure 2.12a) by matching the effective cladding indices so that they are equal. Figure 2.12b shows an image of a fabricated fiber.

It turns out that the birefringence is high enough to reduce the effective index of the fast axis to a value at which the polarization mode is no longer guided. The fiber only guides one single polarization mode within a certain wavelength region depending on the structural parameters. This polarization window is not only affected by the guiding strength ($\sim d/\lambda$) but also by the bending of such a fiber. (Figure 2.13). It shows that the polarizing window can be tailored to the user's requirements, for instance to overlap with the laser bandwidth of an actively doped fiber.

Figure 2.14a shows an actively doped polarizing fiber with an air-cladding to obtain a double clad fiber. The corresponding mode of the core is shown by a near-field image in Figure 2.14b. It combines the low nonlinearity single-mode core with the double clad design, but also features single-polarization properties in the maximum gain wavelength region of short-length Yb-doped fibers. Such a fiber has been applied to laser and amplifier configurations to prove these properties in stable single-mode, high-power laser output [43].

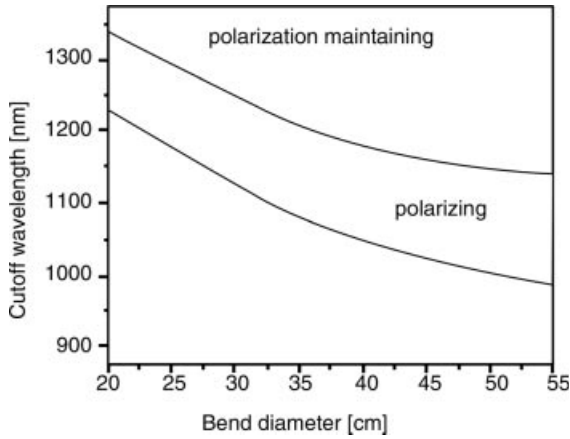


Figure 2.13 Dependence of the polarizing window on the bending diameter.

2.3

Theoretical Description and Nonlinear Effects in Laser Fibers

2.3.1

Propagation and Rate Equation Description

The laser process in fiber amplifiers is described theoretically by combining the local rate equation for the laser process and the power flow (propagation equation) for the fields along the fiber. They have been developed to predict and optimize erbium-doped fiber amplifiers used for telecommunication application [44].

The local rate equation describes the dynamic of the emission and absorption processes of the rare earth ion within its host material by using its spectroscopic

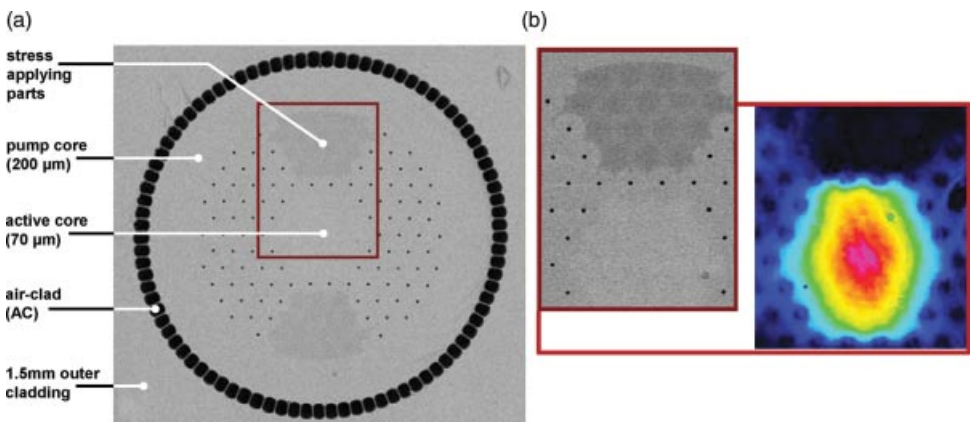


Figure 2.14 (a) Cross-section of the polarizing large-mode-area PCF; (b) corresponding near-field image of the fundamental mode.

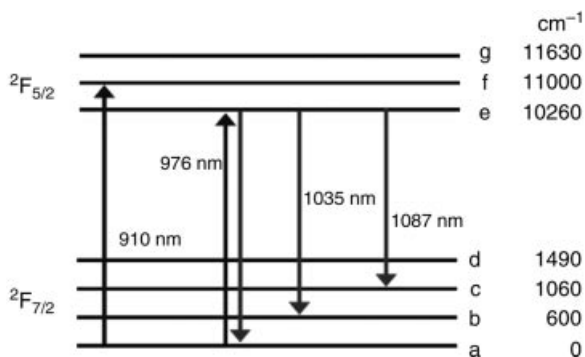


Figure 2.15 Energy level model for ytterbium-ion in fused silica.

properties. Figure 2.15 shows a model for the energy level system for the ytterbium-ion, along with some of the most important emission and absorption lines, which result from the Stark splitting of the upper and lower energy lines. It has been argued that for erbium and ytterbium fibers a reduced two level model for the emission and absorption process can be used so that the effective emission and absorption cross section include the population density and cross section values [44, 45].

Figure 2.16 shows the effective cross sections for emission and absorption $\sigma^{\text{em/abs}}$ of an Yb-doped fiber. Clearly, for a specific fiber, these parameters have to be measured because they are to some extent influenced by the actual core composition – different co-dopants lead to changes in the resulting curve. Especially, phosphor and aluminium influence the absorption peak around 960–980 nm and have been actually used to tailor this property.

Approximations to the full equations given in Reference [44] lead to simplified models. Here we only show a very basic system of equations for the steady-state solution of a single-mode double clad fiber laser or amplifier. Four equations for the forward and backward propagating signal and pump powers $P_{p/s}^{\pm}$ remain:

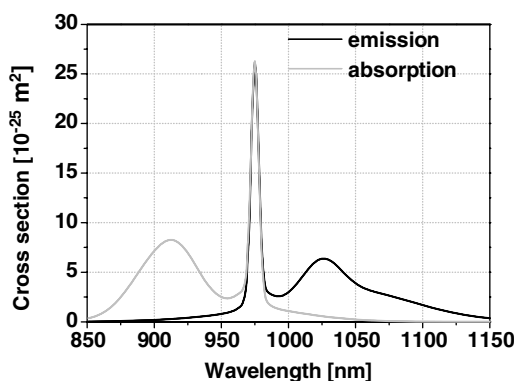


Figure 2.16 Typical emission and absorption cross section of an Yb-doped fiber.

$$\frac{dP_{P/S}^{\pm}}{dz} = \pm \sigma_{P/S}^{\text{em}} \Gamma_{P/S} n_2 P_{P/S}^{\pm} \mp \left(\sigma_{P/S}^{\text{abs}} + \alpha_{P/S} \right) \Gamma_{P/S} n_1 P_{P/S}^{\pm} \quad (2.5)$$

where the total ion density $n_0 = n_1 + n_2$ is the sum of upper and lower population density and $\alpha_{P/S}$ is an additional loss for the fields. Amplified spontaneous emission has been neglected and it is assumed that the pump absorption can be described by a simple overlap factor Γ_p , which is the ratio of doped core area to pump core area ($\Gamma_s = 1$). The upper population density for steady-state conditions is:

$$n_2 = \frac{\frac{\sigma_p^{\text{abs}} n_0}{h\nu_p} \Gamma_p P_p + \frac{\sigma_s^{\text{abs}} n_0}{h\nu_s} P_s}{\frac{(\sigma_p^{\text{abs}} + \sigma_p^{\text{em}}) n_0}{h\nu_p} \Gamma_p P_p + \frac{(\sigma_s^{\text{abs}} + \sigma_s^{\text{em}}) n_0}{h\nu_s} P_s + \frac{1}{\tau}} \quad (2.6)$$

with τ as the upper state lifetime and the total power at a given position $P(z) = P^+(z) + P^-(z)$. The inversion level is defined as n_2/n_0 . Equations 2.5 and 2.6 can be solved not only for fiber amplifiers but also for lasers, if the boundary conditions at the laser mirrors (typically $z = 0, L$) are included in the description for forward and backward propagating fields.

As an example, Figure 2.17 shows the result of such a simulation for a fiber laser with a length of $L = 10$ m. The boundary conditions of an out-coupling mirror with a reflectance of $R_1 = 4\%$ at $z = 0$ and a highly reflectance mirror $R_2 = 99\%$ at $z = L$ has been realized by setting $P_s^-(z = L) = R_2 P_s^+(z = L)$ and $P_s^+(z = 0) = R_1 P_s^-(z = 0)$. The signal wavelength is 1060 nm. The fiber has a pump core diameter of 500 μm and a doped core of 30 μm with an ytterbium doping concentration of 3600 ppm. The fiber is pumped at 976 nm from both sides with $P_p^+(z = 0) = 1000$ W and $P_p^-(z = L) = 1000$ W. The background loss has been set to 0.02 dB m^{-1} . The output power result is $P_s^+(z = 0) = 1800$ W.

Beside the power distribution inside the fiber, Figure 2.17b shows the inversion level along the fiber. It is quite uniform for this example, with an average inversion of $\sim 7\%$. By calculating the dissipated power, which is also shown in the figure, one can realize that on average 25 W m^{-1} of thermal load $d\Phi_{\text{TL}}$ is generated in this example.

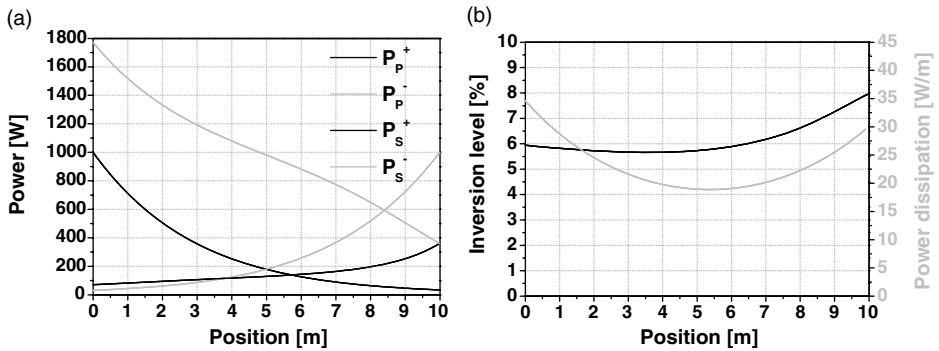


Figure 2.17 (a) Propagating signal and pump powers inside a fiber laser cavity; (b) inversion level and power dissipation along the fiber.

The processes involved in this power loss are the quantum defect, non-radiative decays, and the linear loss introduced into the simulation. It might be that the loss does not contribute to heat generation directly in the core but the level of dissipated power is worth considering when dealing with thermal issues in high-power fiber lasers (see next section).

2.3.2

Thermo-optical Effects

To analyze the thermo-optical properties of fibers heat transfer considerations can be performed [46]. Thermal conduction is the heat transfer process in solid materials, that is, in the fused silica and coating part of a fiber. It is described by $d\Phi_{\text{COND}}$ in Equation 2.7, where k is the thermal conductivity of the material, L the length of the heat flow, dA the cross area of the heat flow, and ΔT the temperature difference. For the heat flow through the cross section of a cylinder with R_2 as the outer and R_1 as the inner radius, which a fiber can be approximated to, Equation 2.8 can be used. For a photonic crystal fiber with an air-clad the conductive heat flow $d\Phi_{\text{COND}}$ through the silica bridges of the air-clad is simply given by Equation 2.9 with N as the number of silica bridges, W_{Bridge} as the bridge width, and L_{Bridge} as the bridge length:

$$d\Phi_{\text{COND}} = k \frac{dA}{L} \Delta T \quad (2.7)$$

$$d\Phi_{\text{COND}}^{\text{Cylinder}} = k \frac{\pi(R_2 + R_1)d\ell}{R_2 - R_1} \Delta T \quad (2.8)$$

$$d\Phi_{\text{COND}}^{\text{AirClad}} = k \frac{NW_{\text{Bridge}}}{L_{\text{Bridge}}} d\ell \cdot \Delta T \quad (2.9)$$

In addition there might be convective and radiative heat flow in the chambers of the air-clad, described by Equation 2.10 and Equation 2.11, where α_k is an empirical value of the thermal conductivity for natural (not forced) convection, with its temperature dependent coefficient C_1 and d as the diameter of the cylinder [47]. Equation 2.11 describes the radiative heat flow by the well-known Stefan–Boltzmann law with $\sigma = 5.6705 \times 10^{-8} \text{ W m}^{-2} \text{ K}^{-4}$ and a typical emission factor for fused silica of $\varepsilon = 0.95$. Actually, due to the small size of the air-chambers, convection is negligible here, but, indeed, the conduction in air of 0.023 W mK^{-1} leads to good heat transport through the air-clad [48]:

$$d\Phi_{\text{CONV}}^{\text{Air}} = \alpha_k dA \cdot \Delta T \text{ with } \alpha_k = C_1 \left(\frac{\Delta T}{d} \right)^{\frac{1}{4}} \quad (2.10)$$

$$d\Phi_{\text{RAD}} = \sigma \varepsilon dA (T_1^4 - T_2^4) \quad (2.11)$$

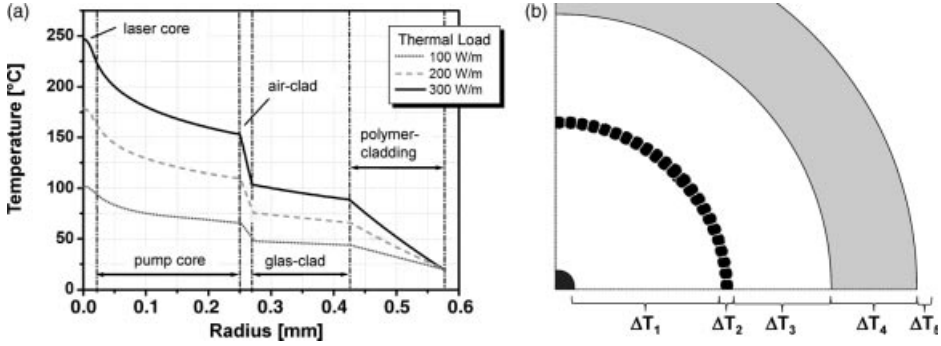


Figure 2.18 Temperature increase within the fiber's cross section for different thermal loads.

Heat dissipation from the coating to the ambient air also involves convective and radiative mechanisms. Therefore, the balance between the thermal load in the fiber's core and the convective and radiative heat flow given in Equation 2.12 determines the temperature difference between the fiber surface and the ambient air (see Figure 2.18b for temperature difference definition ΔT):

$$\begin{aligned}
 d\Phi_{TL} &= d\Phi_{COND}^{InnerClad}(\Delta T_1) = \frac{d\Phi_{COND}^{AirClad}(\Delta T_2) + d\Phi_{RAD}^{AirClad}(\Delta T_2)}{d\Phi_{COND}^{OuterClad}(\Delta T_3)} \\
 &= d\Phi_{COND}^{Coating}(\Delta T_4) = \frac{d\Phi_{CONV}^{Air}(\Delta T_5) + d\Phi_{RAD}^{Air}(\Delta T_5)}{d\Phi_{COND}^{Air}(\Delta T_5)} \quad (2.12)
 \end{aligned}$$

A full finite element analysis of a fiber, which basically solves the same heat transfer equations as discussed, is shown in Figure 2.18 for a fiber with an outer diameter of 850 μm , a pump core of 500 μm , and a core of 30 μm , as well as an acrylate coating with a thickness of 150 μm . The heat load is varied from 100 to 300 W m^{-1} but it is assumed that the heat is efficiently removed on the outer surface to keep a constant temperature. Nevertheless, the outer temperature will not change the gradient inside the fiber and so a temperature increase in the fiber's core above 100 K is obtained for such geometry and at such heat load levels. It also reveals that the air-clad adds some thermal resistance but its influence also in terms of mechanical stability is negligible to first order [49].

From Figure 2.18 it can also be seen that because the heat source is the fiber core a gradient appears within the core itself. Owing to the temperature dependence of the refractive index, this might influence the guiding properties of the fiber. Figure 2.19 shows the situation schematically. An analysis can be made by simulating the guided mode under the influence of such an index deformation [50]. For this analysis it is necessary to introduce an alternative condition for single mode operation as the V-parameter definition does not hold for such a shape. Calculating the overlap of the intensity distribution of the first higher order mode with the core region ($I_{core}/I_{overall}$) is more useful – indeed this parameter is constant for SIF (=0.33) and one-hole missing PCF (=0.52) at the cut-off condition independent of the actual core design

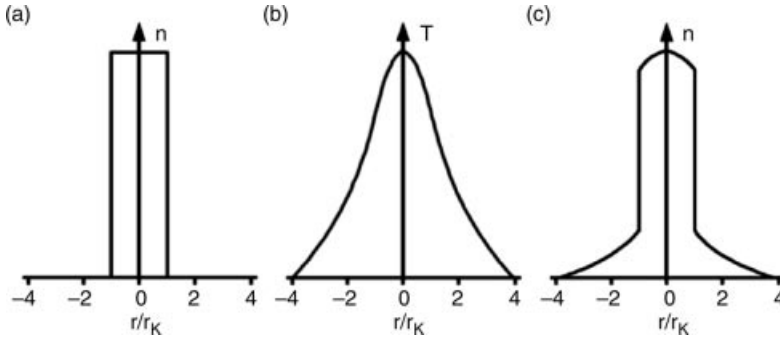


Figure 2.19 (a) Undisturbed index profile of a step index fiber; (b) typical shape of the temperature gradient in a fiber core under laser conditions; (c) influence on fibers core refractive index profile.

(radius, N_A). Therefore, this criterion is used as single-mode to multi-mode transition in the analysis of a step index fiber with $N_A = 0.03$ ($M_{FD} = 30 \mu\text{m}$) shown in Figure 2.20. Illustrated is the overlap of the first higher order mode with the core region (—) and the change of the mode field diameter (---) subject to the thermal load. As shown, with increasing the thermal load the overlap of the LP11 mode increases (the confinement increases) and reaches the single-mode limit at a certain value. The M_{FD} changes to smaller values with a nearly linear slope. Lowering the V -parameter makes the fiber more insensitive to thermally induced refractive index profile deformations. On the other hand, there is a trade-off on lowering the V -parameter at a constant N_A because it also means a lower mode-field diameter and therefore higher nonlinear effects, which will be discussed in the next section. In conclusion of this analysis, for a fiber with given parameters, the thermal lensing

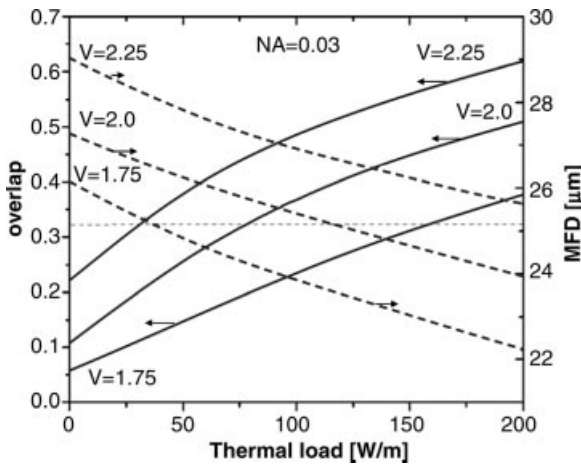


Figure 2.20 Simulated overlap of the LP11 mode with the core region (solid line) and the M_{FD} of the LP01 (---) for a SIF with a N_A of 0.03. The horizontal dotted line is the single-mode condition described in the text.

might influence the fiber performance in terms of higher order modes above a thermal load of 160 W m^{-1} . According to the rate-equations simulation carried out before, this should happen at power levels well above 10 kW .

2.3.3

Inelastic Scattering

With its confinement of light inside a small core and the long propagation length nonlinear optical effects might increase when operating at high power levels. One sort of these nonlinear effects often occurring in continuous wave but also pulsed high-power fiber lasers is stimulated inelastic scattering processes. Brillouin scattering is the interaction of photonic with acoustic phonons while Raman scattering involves optical phonons. These inelastic scattering processes lead to an energy loss of the photon and therefore wavelength shift (Stokes shift). For fiber laser systems, this means a reduction in spectral purity but also power loss and an additional heat load. Here we consider stimulated Raman scattering (SRS), which is described by the propagation equations (2.13), assuming identical effective areas for the different wavelength, where P_S is the power in the Stokes wavelength λ_S , P_P the original signal power at λ_P (pump power for the Stokes field), g_R the Raman gain coefficient, and α_S and α_P the losses at the Stokes and signal wavelength, respectively:

$$\begin{aligned} \frac{dP_S}{dz} &= g_R P_P P_S - \alpha_S P_S \\ \frac{dP_P}{dz} &= -\frac{\omega_P}{\omega_S} g_R P_S P_P - \alpha_P P_P \end{aligned} \quad (2.13)$$

The equations for stimulated Brillouin scattering (SBS) are similar, except that the generated Stokes field is propagating in the other direction. This can be explained by keeping in mind that the acoustic wave (sound) is a local deviation of pressure and therefore density and leads to an optical modulation thanks to the elasto-optical effect. This modulation can be seen as a moving grating Doppler-shifting and reflecting the optical field. Furthermore, the Brillouin gain is 500 times smaller than the SRS gain.

The physical origin of inelastic Raman scattering is the excitation of molecular vibrations. Practically, the wavelength of the propagating signal is shifted and power is lost. With some photons already generated at the Raman wavelength, the process can be stimulated and converts (depletes) a large amount of the signal (the term $\sim g_R P_S$ is large in Equation 2.13). From the above equations and some approximations, one can derive a threshold power at which this conversion manifests [51]:

$$P_{\text{SRS}}^{\text{threshold}} \sim 16 \frac{A_{\text{eff}}}{g_R L_{\text{eff}}} \quad (2.14)$$

Solving the Equation 2.13 numerically visualizes this situation. The results are shown in Figure 2.21, where a passive lossless fiber is assumed. For a power below the threshold, the light can propagate undisturbed through the fiber (Figure 2.21a). Above the threshold, the signal is converted into the first Stokes wave at a position

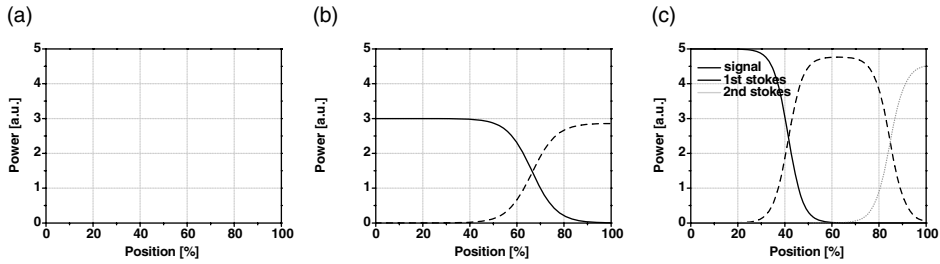


Figure 2.21 Simulation of SRS in a lossless fiber with signal input at $z = 0$: (a) signal power below threshold, (b) above threshold for generating 1st Stokes, and (c) strong signal to generate 2nd Stokes.

determined by the precise power level (Figure 2.21b). At higher power levels, this first Stokes might generate a second Stokes with respect to the original signal as shown in Figure 2.21c. In addition power is lost due to the quantum defect even in this lossless situation.

Figure 2.22 shows an experimental proof of this. A CW fiber laser at 1062 nm with an average power of 10 W is coupled into a 1.6-km long passive single mode fiber. The spectrum versus the input power is shown in Figure 2.22a. As one can see, at a relatively low power of 0.75 W, a new spectral component at 1120 nm is generated. Increasing the power to 5 W leads to the generation up to the fifth Stokes and a power generated up to a wavelength around 1500 nm. Above that power level, no individual lines can be observed due to the interplay of further linear and nonlinear effects. The spectral picture is again analyzed in Figure 2.22b, which show a good qualitative agreement with the simulation above with respect to total conversion to the next higher Stokes.

For the design of fiber laser systems, SRS has to be considered and the equations have to be combined with the propagation equations (2.13) to account for additional gain due to the laser process and spontaneous photons through ASE. One then can end up with better prediction of the Raman threshold [52].

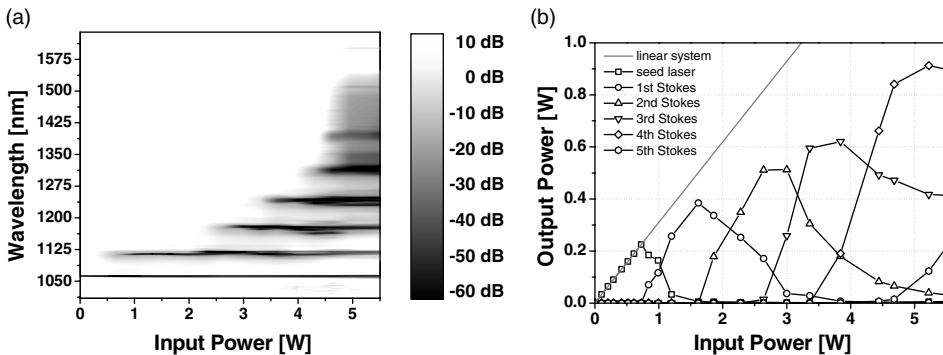


Figure 2.22 (a) Experimental spectrum at the output of the fiber, depending on input power, and (b) its integrated powers for each spectral line.

2.3.4

Self-Phase Modulation

Another nonlinear effect encountered in fibers is the Kerr effect – the intensity dependence of the refractive index covered by Equation 2.15. There, n_2 is the nonlinear refractive index that is of the order of $3 \times 10^{-20} \text{ m}^2 \text{ W}^{-1}$ for fused silica:

$$n = n_0 + n_2 I \quad (2.15)$$

Owing to the instantaneous nature of this effect, an intensity variation over time will lead to a phase change and, consequently, to an instantaneous frequency shift. With the scalar optical field amplitude $A(T) = \sqrt{P} e^{i\phi(T)}$, the frequency change $d\omega/dz$ is covered by Equation 2.16, where γ is the nonlinear coefficient:

$$\begin{aligned} \frac{d\omega}{dz} &= -\gamma |A(z, T)|^2 \\ \gamma &= \frac{n_2 \omega_0}{c A_{\text{eff}}} \end{aligned} \quad (2.16)$$

While this effect plays an important role for short pulse lasers and amplifiers due to the temporal profile of the pulses and their high peak powers, it will also lead to spectral changes for CW radiation. Practically, there are two kinds of spectral changes that are usually recognized experimentally. Firstly, a spectral broadening appears on the output signal with increasing power and, secondly, the generation of sidebands. Both situations are not directly obvious by taking a CW field with $\phi(T) = 0$ in Equation 2.16, because it would only acquire a constant phase change and therefore no frequency change during propagation along the fiber. However, a steady-state analysis of the extended propagation equation, the nonlinear Schrödinger equation, including dispersion reveals that for anomalous dispersion fibers the signal is inherently unstable and spectral sidebands are generated that grow exponentially with propagation distance. This effect is called modulation instability and leads to the break-up of the signal into pulses in the temporal domain [53, 54]. However, in the case of Yb-doped fibers operating in the 1.0–1.1 μm region, normal dispersion is present and modulation instabilities are only observed, if two polarizations interact by cross-phase modulation [55]. In addition to this sideband generation, spectral broadening is observed and is a consequence of any intensity fluctuations that might already exist due to the finite spectral bandwidth of the propagating signal. An experimental example is shown in Figure 2.23 and confirms that this effect has to be considered even for the amplification of CW sources.

2.3.5

Mode Instabilities

If a fiber laser or amplifier with a core close to the cut-off ($V \geq 2.4$) is operated, the output is typically the fundamental mode with a beam quality close to that of a Gaussian beam. Deviation from this may result from the core design especially for

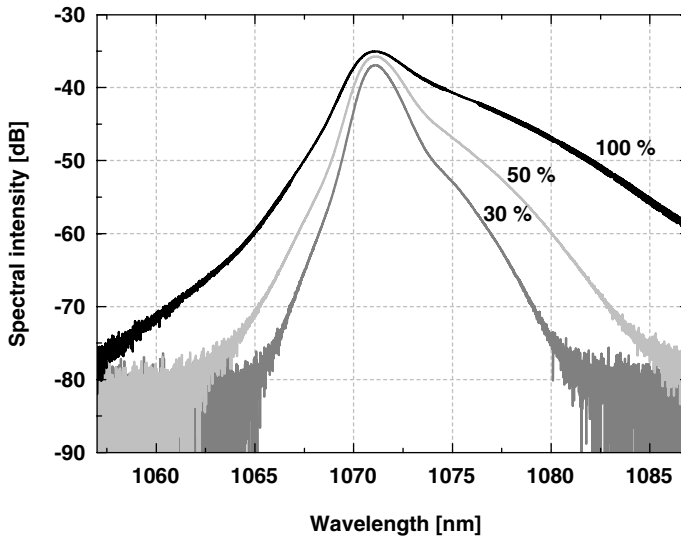


Figure 2.23 Spectral broadening of a CW laser during amplification in a fiber for different normalized power levels.

the photonic crystal fiber design [56]. However, in all these cases one would expect that the beam quality is power independent for output powers below the thermal lensing limit discussed in the previous sections. Unfortunately, an unusual mode instability has been observed experimentally for fibers close to (or slightly above) the single-mode cut-off. The mode instability can be observed in high-average power operation of fiber lasers and amplifiers when the amplified signal power exceeds a certain threshold value. Below this threshold, the near field profile and the measured beam quality out of the amplifier fiber appears to be single mode. However, above the threshold an apparently random temporal change in the mode content accompanied by a sudden decrease in beam quality can be observed. A reduction to a power level below threshold results again in a stable fundamental-mode output beam, thus, no hysteresis is observed. Furthermore, the average power does not drop at this threshold and can actually be further increased with subsequent beam quality degradation. The frequency of the modal fluctuations is typically lowest (some Hertz) at the threshold and increases up to the kHz-level when the pump power is further raised. Further experiments showed that for a given fiber design the threshold occurs at comparable (but not identical) power levels for either continuous wave or pulsed operation, which in principle rules out any strong dependence of this effect on the peak power. Further details on experiments where this effect has been observed can be found in Reference [57] for continuous wave and in Reference [58] for pulsed amplification in the *same* fiber.

Two experimental results of the measured M^2 -value (2nd momentum method) as a function of signal output power are shown in Figure 2.24 for two double clad fibers used in amplifier configuration with a CW-seed. The first fiber is a PCF with a core

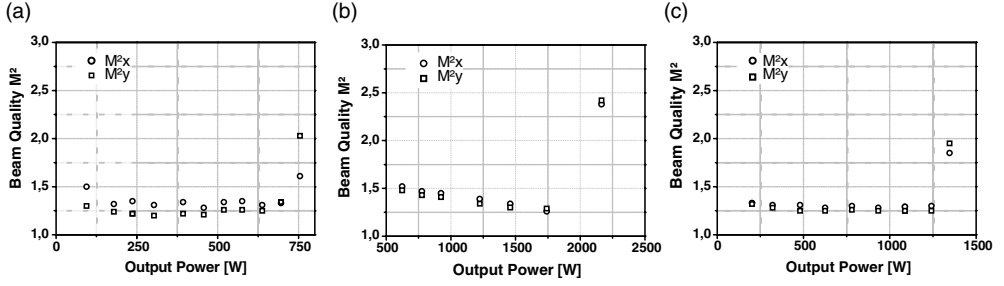


Figure 2.24 Measured beam quality M^2 (2nd moment method) as a function of the output signal power for a PCF (a) and SIF [(b) and (c)] CW-amplifier (see text for details). The beam quality degradation resulting from the onset of mode instabilities can be seen for the highest power.

that is defined by a seven missing air-holes microstructured region with a M_{FD} of $33\text{ }\mu\text{m}$. The second fiber is a step-index core fiber with a M_{FD} of $27\text{ }\mu\text{m}$. Both fibers have an air-clad with a diameter of $500\text{ }\mu\text{m}$ and are pumped in the counter-propagating direction at 976 nm central wavelength. Figure 2.24a shows the measurement for the 10.5-m long PCF. The seed signal is a narrow band (12 pm FWHM) amplified spontaneous emission source at 1030 nm central wavelength (please see Reference [57] and Section 2.5 for more details). The threshold-like onset of mode instabilities can be clearly observed as a sudden increase of the M^2 factor from 1.3 to 1.8 at an output power of about 700 W . Figure 2.24b and c shows the measurement for the 9.5-m long SIF for two different seed sources [59]. The applied signal powers are 20 W at a wavelength of 1055 nm (narrow band $\Delta\lambda \approx 60\text{ pm}$, linearly polarized) in Figure 2.24b and 200 W at 1071 nm (broad band $\Delta\lambda \approx 2.6\text{ nm}$, unpolarized) average seed power in Figure 2.24c. The measured mode-instability threshold is 1240 W for the 20 W seed average power and 1740 W for the 200 W seed. An additional experimental threshold of 950 W was obtained for 8 m of the same SIF from Reference [58] for the amplification of a quasi-CW (80 MHz) signal comprising broadband pulses. In this experiment, 30 W of linearly polarized seed power centered at 1040 nm wavelength was used.

The increase of the mode-instability threshold with a change of the seed source as indicated in Figure 2.24b is a remarkable feature. Since changing the seed power and wavelength primarily affects the inversion along the fiber, the results presented in Figure 2.24b strongly suggest that these instabilities are linked to gain dynamics. Figure 2.24 also shows that below the threshold the beam quality steadily improves with increasing pump power. The reason for this effect is that the residual signal light that is not coupled into the signal core (free space coupling) and is guided in the pump cladding degrades the measured M^2 values. However, the relative fraction of this light decreases with increasing signal power and, therefore, the M^2 measurement is improved.

As a conclusion of these preliminary experiments (and also of additional experiments not shown here) it can be stated that the mode-instability threshold is influenced by several experimental parameters such as the wavelength, seed power, the quality of the mode excitation, the temporal and the spectral properties of signal

and pump, the signal polarization, and so on. By comparing additional fibers (details not shown here) it can be summarized that the observed threshold value varies between a few hundred watts and several kilowatts of average power depending on the actual fiber design, that is, the core size, the number and losses of HOMs, and the fiber length. In these experiments it has been observed that the threshold is, under comparable experimental conditions, typically lower for larger mode field diameters.

The physical cause of the observed mode instabilities is not completely understood yet. In principle the experimental observations exclude “classical” nonlinear effects, since it seems that the threshold is primarily dependent on the average power and not on the peak power. Additionally, the onset of instabilities only observed at high average-power levels (i.e., they have not been observed in low power experiments with the same fibers and the same gain) suggests that they can be attributed to saturation effects, thermal load, and/or induced stress. However, a complete theoretical description of this problem would require a three-dimensional analysis of a high-power fiber amplifier, including the temporally and spatially resolved description of the gain dynamics, modeling of the thermal load and stress, and calculation of the beam propagation and deformation along the fiber core. If this exhaustive modeling were possible, it would certainly rely on demanding numerical simulations that have yet to be developed.

Nevertheless, some initial, but not final, explanations are available. After mode instabilities have been observed at high average-power levels, they were attributed to transversal spatial-hole burning (TSHB) [60]. Here, the fundamental mode depletes the inversion only in the inner part of the doped region of the core. The remaining inversion in the outer regions of the core can preferentially amplify HOMs possessing their intensity maximum in that area. However, simulations based on a spatially resolved solution of the steady-state rate equations predict that the fundamental mode always experiences a higher gain than the HOMs in fibers with confined doping. This is especially the case for many actively-doped PCFs, since PCFs usually possess a doping radius smaller than the core radius as a result of the stack-and-draw production technique. Therefore, TSHB cannot be the only mechanism and cannot explain the threshold-like behavior since it would only predict a steady degradation of the beam quality. The most likely explanation of this mode-instability effect is the formation of induced long-period gratings [61]. Here the interference pattern of the fundamental mode and a HOM is mapped into the inversion that, in turn, locally modifies the refractive index of the core. In theory, the resulting long-period grating can efficiently couple the light from the fundamental mode to HOMs. Moreover, this type of induced gratings has already been experimentally demonstrated by exploiting the Kerr effect [62]. Additionally, inversion related gratings that are induced by counter-propagating signal waves have been known for many years [63]. In the case of the inversion gratings that may be responsible for the observed mode instabilities, the exact origin of the index change still has to be determined. Possible causes are the resonantly enhanced nonlinearity [64] due to the inversion, the temperature dependence of the refractive index, or the induced stress. While further theoretical investigations have been carried out [65], a deeper analysis is necessary for a complete understanding of this effect.

2.4

Fiber Components for High-Power Fiber Lasers

2.4.1

Fiber Preparation

For the assembly of a fiber laser system the components usually have to be prepared and joined. The most common joining technology for fibers is splicing using a heat source melting the fiber and bringing it into contact with another fiber or component [66]. This ensures mechanical stability and the lowest loss for the propagating light. The splicing concept has been developed to perfection for commercial devices for telecom applications, with fibers with outer diameters of $125\text{ }\mu\text{m}$ (Figure 2.25). The heat is, typically, generated by electrodes or filaments, but flames are also used for special applications.

Before the splicing process for joining two fibers is started, the fiber coating is typically removed and the fibers are mechanically cleaved by applying tension to the fiber and initiating a fracture by intrusion of a diamond blade. This cleaving is preferred to polishing due to its fast processing and the cleanliness of the fiber

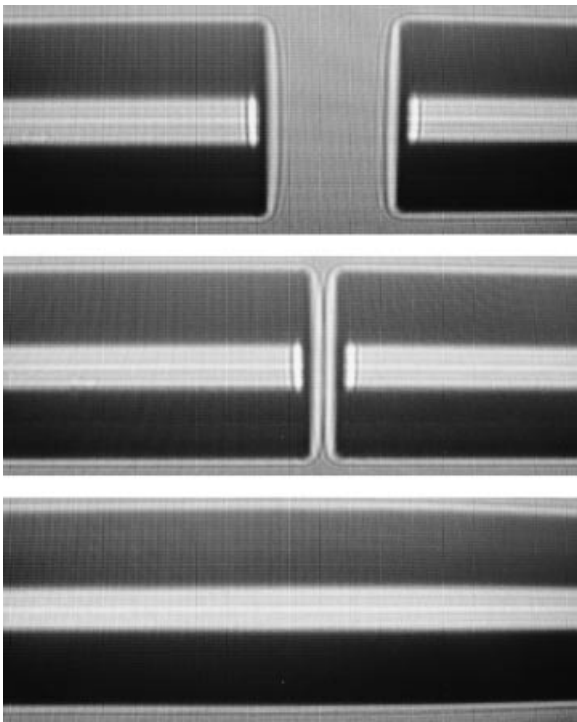


Figure 2.25 Image of a splicing process for two identical fibers from top to bottom: alignment, closing gap, and final splice after melting and contacting the fibers.

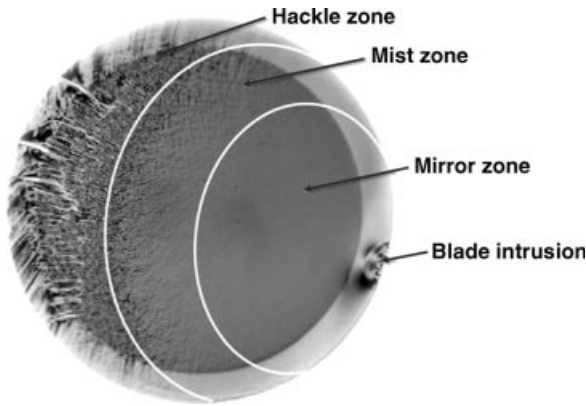


Figure 2.26 Microscopic image of a mechanically induced fiber cleave and its possible result in terms of surface quality.

end-face. However, it has to be controlled very precisely to ensure a high quality surface and the right cleave angle, which is a strong requirement for a low-loss splice. Figure 2.26 shows an example of the three surface qualities that can develop while cleaving:

- **Mirror zone:** high quality of surface comparable to a polished fiber.
- **Mist zone:** transition region to hackle zone formed by different crack fronts.
- **Hackle zone:** develops due to different crack fronts that are generated if the kinetic energy increases. This energy increase cannot be handled by a single crack front, which is determined by a specific velocity. A rough surface is formed due to interference and different height levels of propagation for the crack front.

With the right cleave parameters, only the mirror zone is obtained.

Beside the splicing process, other manipulations of the fiber might be required for fiber laser systems. Figure 2.27 shows the variety of applications for a laser-based heat source, which can be a CO_2 laser, that is greatly absorbed by fused silica. The examples shown in this figure are:

- Partial collapse of air holes in PCF to prepare the fiber for better cleave quality; typically, the cleave quality of a non-collapsed air-hole PCF is poor due to interruption of the crack by the holes;
- thermal induced removal of the polymer coating, thereby avoiding mechanical removal that might harm the fiber surface by mechanical scratches;
- shaping of fibers for beam deformation or micro-optical elements;
- thermal induced cleaning of the surface before further processing;
- tapering of fiber for geometrical adaption such as mode-field adapters;
- endcap preparation, for example, to reduce the intensity at the fiber-to-air interface.

The important endcap preparation is discussed in detail in the next section.

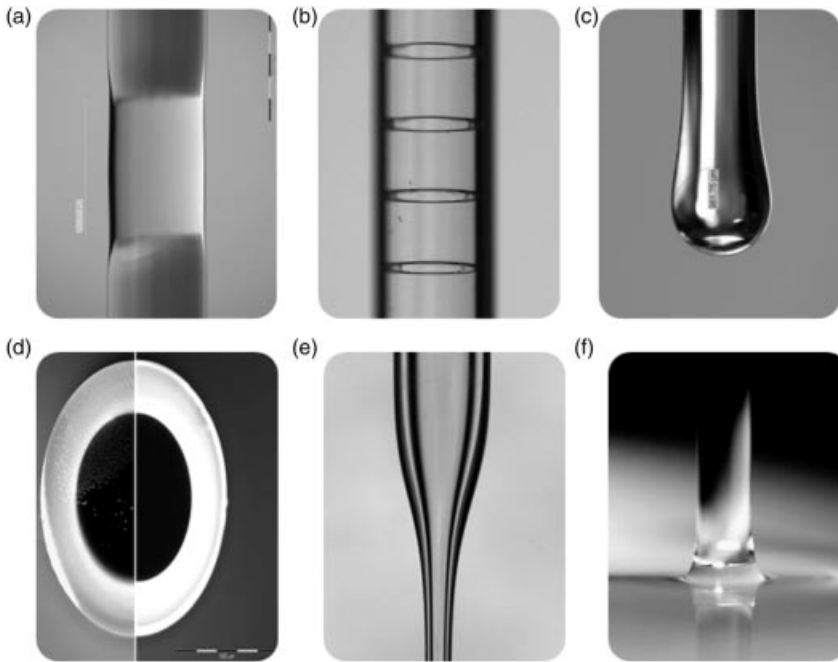


Figure 2.27 Application examples of laser-based fiber preparation: (a) partial collapsing of PCF, (b) removal of coating, (c) shaping by melting, (d) thermal induced cleaning, (e) tapering, and (f) endcapping.

2.4.2

Endcaps

Endcaps are fused silica elements without guiding structures (core-less) attached to a fiber of similar material. The reasons for them are manifold, for instance:

- protection of the fiber tip, especially closing holes and protecting PCFs;
- ease of cleaning the fiber end;
- easier application of coatings to larger surfaces;
- holding structure in connectors;
- reduction of intensity for the beam exist by beam expansion inside the endcap (Figure 2.28);
- beam shaping by applying optical elements as endcaps.

While there are several reasons for connecting endcaps to fibers, the method applied is normally derived from fiber splicing through partially melting and attaching the components. An elegant heat source is the already mentioned CO_2 laser [67]. Figure 2.29a shows an example of an endcap laser spliced to a passive transport fiber. The close-up view in Figure 2.29b show the concave fillet weld formed

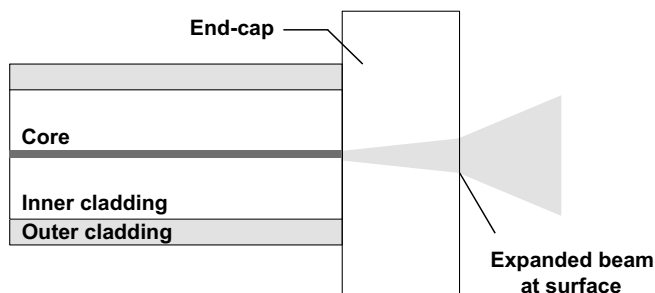


Figure 2.28 Schematic illustration of an endcapped fiber to reduce the intensity out of the fiber.

after melting and freezing the glass. The treatment of PCF requires special handling, with some significant differences compared to standard fibers. Features like air-clad structures, highly rare-earth doped cores with low N_A , and stress applying parts of the PCFs as discussed in Section 2.2 require additional steps in fiber preparation. For instance, CO_2 laser splicing can be used for a defined air clad collapsing and endcap splicing to obtain a stable and sealed fiber end-face while preserving high beam quality and additional functionality (Figure 2.29c and d). Care has to be taken if endcaps are attached to PCFs, because the length of the collapsed region might influence the beam quality. The reason for this is the interrupted guidance for collapsed air-holes so that the beam might interfere with additional elements like the stress-applying parts discussed in Section 2.2.4.

2.4.3

Pump Coupler

As the demand for integrated high-power laser systems has increased, much research efforts have been focused on packaging and integration of laser systems into single units including pumping and amplifying. Recent investigations using

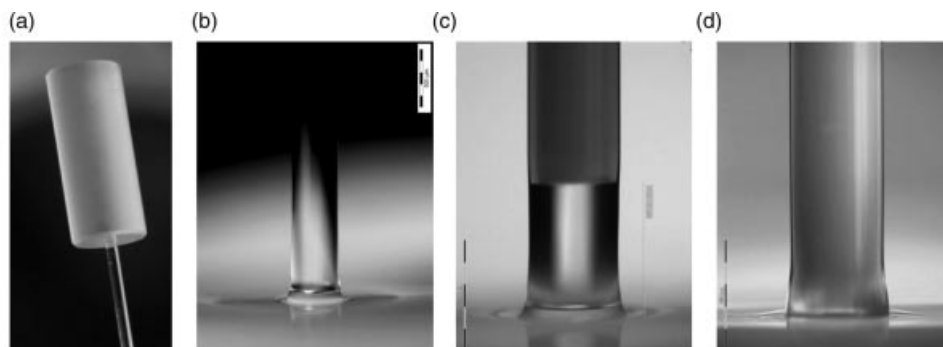


Figure 2.29 Fused silica block spliced to a passive transport fiber (a) and a close up of the splice region including the concave fillet weld (b); close up of a PCF showing a collapse of the air-cladding 700 μm in length (c), and improved splice with a collapse of $< 100 \mu\text{m}$ (d).

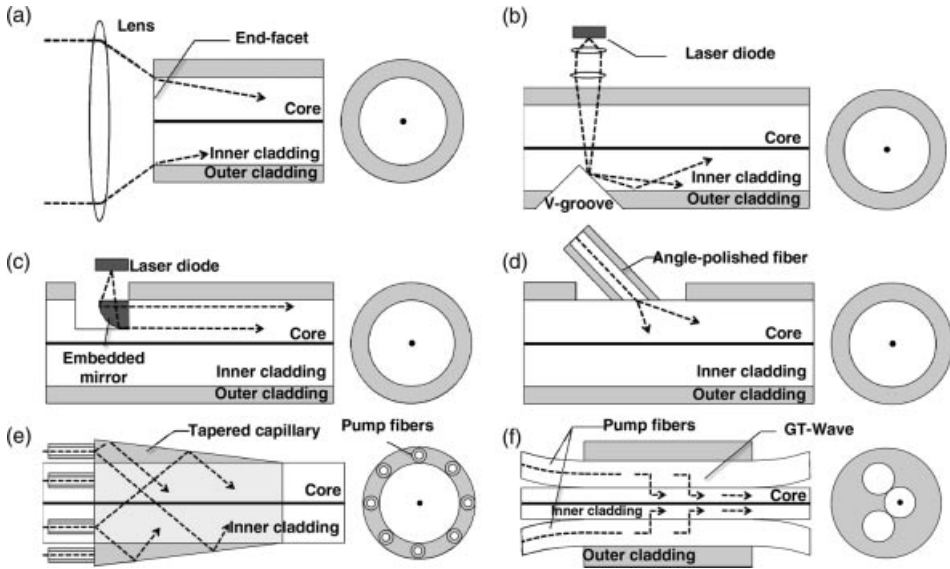


Figure 2.30 Pump coupling schemes: (a) free-space end-facet, (b) V-groove approach, (c) embedded mirror, (d) angle-polished fiber, (e) tapered capillary, and (f) GT-wave concept.

integrated fiber optics have led to various compact, reliable, and efficient high-power fiber laser systems for fundamental as well as industrial applications [68–71]. Especially, the development of the all fiber pumping concepts has been a key issue not only for scaling of the output power of fiber lasers but also for minimizing system size and the cost of high-power fiber laser systems. Thus, continuous efforts have been made to integrate and combine lasing and pumping units in high-power fiber laser systems.

In the laboratory a free space coupling scheme is often used to end-pump a double clad fiber (Figure 2.30a). With the right coupling optics, the etendue of the pump core can be used in the most efficient way, because the numerical aperture and spot diameter of the focusing optics are matched to the pump core parameters. However, to be able to use the ends of the fiber for further signal delivery, the pump light has to access the pump core sidewise (side pumping). This has been achieved through side coupling methods, which rely on polishing or peeling off the pump cladding, such as the V-groove side-coupling (Figure 2.30b) [72], the embedded-mirror (Figure 2.30c) [73], using an angle-polished fiber (Figure 2.30d) [74], or related capillary methods (Figure 2.30e) [75, 76]. These methods suffer from mechanical instabilities, low power handling capacity due to adhesives, or reduced reliability potentially caused by partly damaged fibers. Other approaches used pump fibers that are fused and/or tapered to match the pump core while the signal light might be fed through this arrangement [77–79]. Furthermore, techniques that are currently used in commercial fiber laser systems are based on having the pump fibers in contact with the pump core along a certain length of the fiber and thus having a kind of side-coupling arrangement over a longer interaction length [80, 81]. These approaches have again the advantage of freely usable fiber end-facets

(Figure 2.30f). A drawback of these later methods is the limited design flexibility of the pump core area, which is to first order given by the sum of pump fiber and pump core areas and thus determines the absorption length.

Beside these methods, a combination of multiple pump fibers and discrete coupling optics in a miniaturized, monolithic all-glass pump combining scheme is possible. It is based on the idea of surrounding the active double clad fiber with several pump fibers that are imaged to the pump core by a reflector. To achieve a monolithic device, all components are spliced and the reflector is given by the inner surface of a coated lens [82]. Realizations of this scheme have been done by metallic hollow reflectors. Here a hole in the center of the reflector separated the exiting laser beam from the fibers active core. One drawback of this method is that the active fiber needs to be polished at an angle that prevents back reflections to the amplifier, which makes the alignment of the hole relative to the emission cone difficult. In contrast, realization is also possible by adopting a dichroic coated lens to achieve a high reflection and coupling efficiency for the pump light, while the laser light is transmitted [83]. Splicing the lens to the fibers avoids angle polishing and critical alignment. Additionally, this lens serves as a protecting endcap for high power or high energy generation. Figure 2.31 shows schematically the proposed device, which consists of a dichroic coated planar convex lens and a rare-earth doped double-clad fiber surrounded by multiple pump fibers. The pump light exits from the pump fibers and is imaged into the pump core of the actively-doped double clad fiber by reflection at the second, concave surface of the planar convex lens, which is coated for high reflectance at the pumping wavelength. The dichromatic coating of the lens makes it possible to propagate the amplified signal for further use, since the coating of the lens surface shows high transmittance at the lasing wavelength. Notably, firstly, the signal beam can expand by propagation in the lens and exit with lower intensity at the lens compared to the fiber turning this lens into a protective endcap. Secondly, the dichroic and geometrical arrangement protects the pump diodes from laser light to a high level. The proposed scheme could be applicable to almost all kinds of fiber laser systems that utilize pump fiber and amplified fiber devices with free space output.

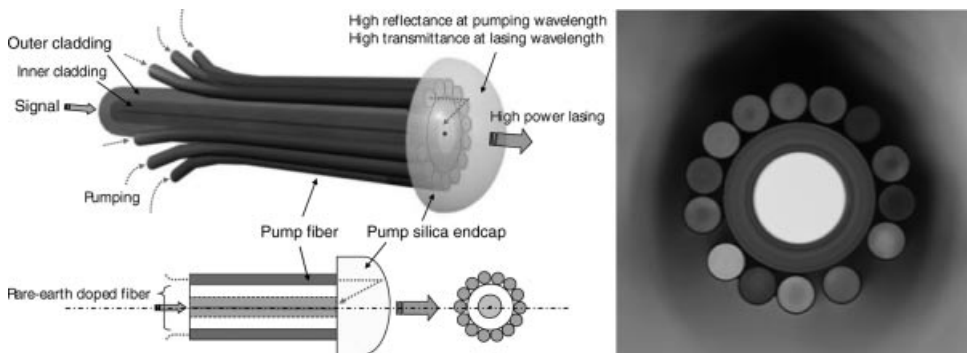


Figure 2.31 Monolithic all-glass pump combiner scheme and front view of a typical realized arrangement.

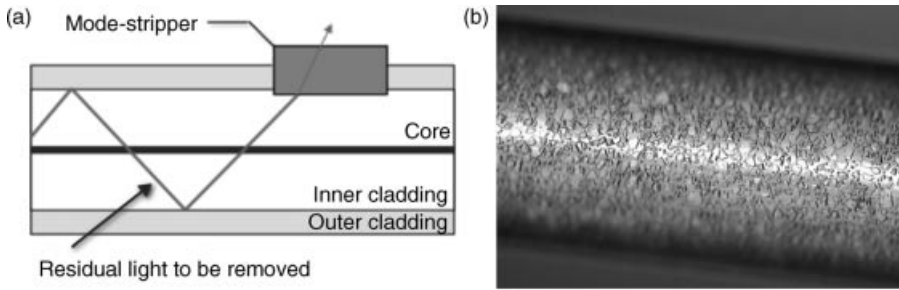


Figure 2.32 Illustration of a mode-stripper (a) and realization by an etched fiber surface (b).

2.4.4

Mode-Stripper

In many situations of fiber integrated devices using double clad fibers, some residual or unwanted light has to be removed from the inner cladding of the fiber. For instance, residual pump light from a pump core of a fiber amplifier has to be removed before the signal delivery fiber. Another example is the slicing of single mode cores that have to withstand high power levels so that even small coupling losses have to be removed efficiently in order not to harm the fiber or coating. The method used to remove unwanted light is the application of a mode-stripper (Figure 2.32a). A mode-stripping element is attached to the fiber to absorb, scatter, or bend the unwanted rays of light. Besides absorbing materials, transparent materials of similar or higher refractive index to that of the inner cladding can be used to alter the total internal reflection and hinder further propagation. These materials, especially when based on organic glues, have the drawback of being power limiting as they usually have a low acceptable maximum temperature limit. Alternatively, the surface can be modified without additional material layers. This can be achieved for instance by a wet-etching process using hydrofluoric acid (HF), which leads to a rough surface due to a combination of impurities varying the local etching rate and the recrystallization of the etched components. Figure 2.32b shows an image of an etched fiber surface. As a result, the light is scattered off when hitting the surface without heating it locally and so this is a convenient process used for high-power fiber lasers.

2.5

High-Power Experiments

2.5.1

Narrow Linewidth CW Amplification

Figure 2.33a shows the schematic setup for most fiber amplifiers, consisting of a seed source, an amplifier fiber, and a pump source. With the pump counter propagating in the direction of the seed source, the output and pump radiation is separated by a

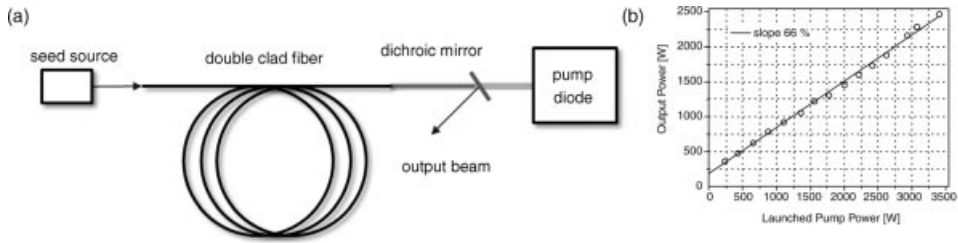


Figure 2.33 Schematic setup of a fiber amplifier pumped in the counter-propagating direction (a) and typical output characteristic for the high-power fiber amplifier (b).

dichroic filter unless a pumping scheme is used with other methods of beam delivery after the amplification (Section 2.4.3). A typical result of the performance is shown in Figure 2.33b, where the output power is plotted against the launched pump power, resulting in a linear slope of 66%. In contrast to lasers, the slope starts at the seed power through the fiber without pump; in this case a 350 W fiber laser has been used as a seed source. The fiber consists of a cladding pumped non-polarizing Yb-doped photonic crystal fiber having a 42 μm core diameter (33 μm M_{FD}) and 500 μm pump core diameter similar (but not identical) to the fiber shown in Figure 2.11d. To date, the output power of 2500 W is the highest published result from an air-clad photonic crystal fiber. However, the seed source had a bandwidth of several nm and the beam consists of several transversal modes at high power levels due to the mode instabilities discussed in Section 2.3.5.

2.5.1.1 Narrow Linewidth Amplification of a Broadened Single-Frequency Diode Laser

For several applications, for instance the beam combining method that will be discussed in Section 2.5.3, narrow linewidth high-power sources are required. The setup can be easily changed by using a narrow linewidth seed source. For the experimental results shown in Figures 2.34 and 2.35, the seed source consists of a tunable external cavity diode laser (ECDL) of maximum output power of ~ 35 mW running at ~ 1055 nm. A two stage fiber pre-amplifier is used to amplify the signal to a power level of ~ 20 W linear polarized light used for further amplification. The pre-amplifier is 60 dB isolated from the following main amplifier. The main amplifier fiber is a cladding pumped non-polarizing Yb-doped nanostructured step-index fiber having a 22 μm core diameter (27 μm M_{FD}) and 500 μm pump core diameter, which is pumped with a fiber coupled pump diode at 976 nm. A half-wave plate at the main amplifier's entrance is used to adjust the orientation of the linearly polarized seed-signal after the isolator. An output power of 1350 W is obtained with a slope efficiency of 66%. The beam quality measurement has already been shown in Figure 2.24b, where a mode-instability appears at an output power of 1250 W. Up to this power level the degree of polarization is reasonably good ($\text{DOP} > 92\%$) even without polarization elements in the fiber design. To prevent SBS, the ECDL signal is broadened by broadband current modulation, leading to a phase and amplitude modulation of the signal. The resulting intensity fluctuation led to a slight spectral broadening from 71 to 78 pm by self-phase modulation, experimentally confirmed in Figure 2.35. If one

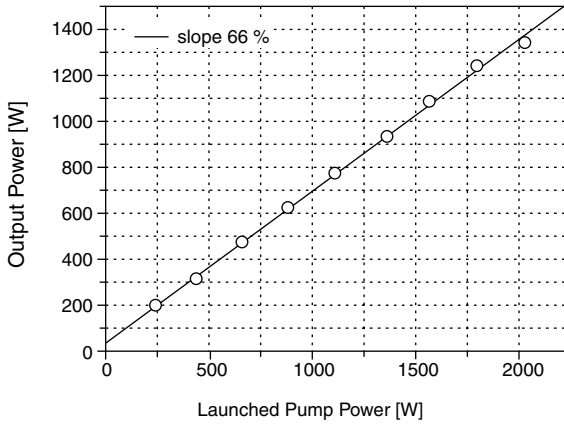


Figure 2.34 Power output characteristic for a high-power narrow linewidth fiber amplifier (see text for details).

reduces the modulation of the seed laser, SBS can be observed, so that a further narrowing of the signal at this power level was not possible.

2.5.1.2 Narrow Linewidth Amplified Spontaneous Emission Source

As a conclusion to the experimental results, SBS is one of the major problems that occur while power scaling narrow linewidth signals even for advanced fiber designs. Over recent years methods for effective SBS suppression have been proposed, which can be categorized basically into two classes: those that influence fiber parameters and those related to the signal itself. For instance, a suppression of 4.3 dB can be reached by implementing special acoustically anti-guiding fibers [84]. In addition, by varying fiber parameters such as strain, temperature, or core radius along the fiber length a certain degree of SBS suppression can be reached [85]. A proven method to modify the signal is the sinusoidal phase modulation of a narrow-band signal to

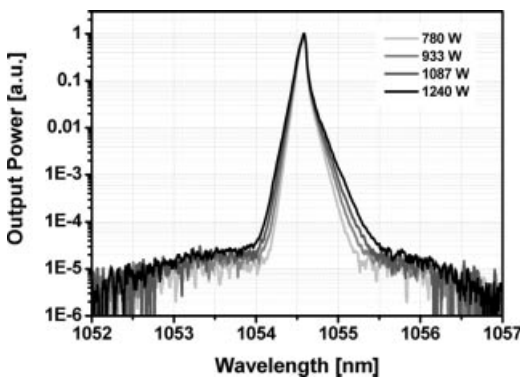


Figure 2.35 Spectral broadening of a narrow linewidth source when amplified in a fiber. From outer to inner the lines correspond to 1240, 1087, 933, and 780 W, respectively.

generate several sidebands with a spectral separation of at least two times the gain bandwidth of SBS (~ 30 MHz) [86]. But in this case the accentuated peaks of the sidebands can still trigger SBS and even the broadband modulation used in the experiment described before might not prevent SBS. When using ASE no longitudinal modes or sidebands are present but the photons are equally distributed within the spectral shape (e.g., Gaussian) making SBS most unlikely. In the following the ASE source used is described, which possesses a measured coherence length of 56 mm, which corresponds to a FWHM bandwidth of only 12 ± 2 pm (3.5 ± 0.6 GHz), respectively.

The experimental setup can be split into two functionally different parts, a low-power all-fiber ASE front-end source that molds the spectrum into its final shape and a free-space two-stage amplifier section. The all-fiber front-end source has the advantage of being highly immune from external influences like stress and temperature and is therefore most important for long-term reliable CW-output. When setting up an ASE source, any cavity build-up has to be eliminated to avoid lasing. Generally, active (especially core-pumped) fibers can have a very high gain. Thus, parasitic cavities will easily lead to laser activity and probably to self-pulsing as well [87, 88]. For a setup including spliced all-fiber components it is only possible to minimize but not to avoid the oscillation of a certain number of longitudinal modes due to inherent small back reflections and/or Rayleigh scattered signal light. If the reflectivity becomes too high the lasing threshold can be reached, leading to a perturbed ASE generation process at a certain pump level. This can easily be the case when using highly reflective fiber Bragg gratings (FBGs) with the intention to spectrally confine the output spectrum. To avoid this generation, spectral shaping by means of two FBG and amplification of the ASE light is carried out separately. Strong optical isolation between these three stages successfully prevented mutual interactions. In the experimental setup (Figure 2.36) all active and passive fibers are polarization-maintaining single-clad transversal single-mode fibers with a M_{FD} of $\sim 7 \mu\text{m}$. The single-mode pump laser diode (SM-LD1) at 976 nm is wavelength stabilized by a FBG and additionally includes current and temperature control. It is split equally (50 : 50), leaving 200 mW for each pump transmission port (P) of the

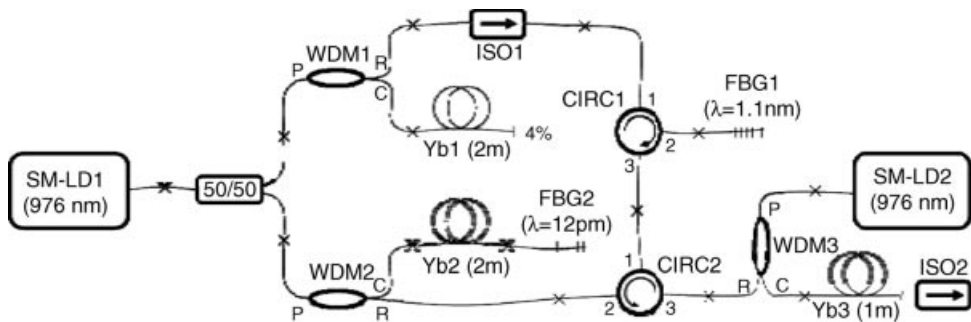


Figure 2.36 Scheme of the experimental setup of the all-fiber ASE front-end, which reduces the spectral bandwidth iteratively down to ~ 12 pm by means of two FBGs. The final output power after ISO2 is 400 mW at a center wavelength of 1030 nm.

wavelength division multiplexers WDM1 and WDM2. In the first 2-m long Yb-doped core-pumped fiber (Yb1), which is spliced to the common port (C) of WDM1, a 10 nm broad ASE spectrum reaching from 1025 to 1035 nm is generated. In this crucial section the (4%) Fresnel reflection of one fiber end-facet is used to increase the output power at the reflection port (R) of WDM1 up to 20 mW while staying below the laser threshold. An isolator (ISO1) and the first transition within circulator 1 (CIRC1) is used to isolate the ASE generation process by at least 70 dB. Notably, substituting the Fresnel reflection by a high reflective FBG as well as leaving out ISO1 leads to the described self-pulsing behavior. FBG1 has a reflectivity of >90% and reduces the bandwidth by a factor of ~ 10 down to about 1 nm. The remaining power is subsequently 70 dB-isolated by two further circulator transitions and sent to the double pass configuration of the second Yb-doped fiber (Yb2). This core-pumped fiber, which is also 2-m long, amplifies the remaining signal power of 140 μ W in a first pass. The relatively small reflectance (32%) of FBG2 and the further reduction of the spectral width down to ~ 12 pm leads to a low but sufficient seed signal power for the second (counter-propagating) amplification pass through fiber Yb2. The overall gain of this double pass amplifier (including losses caused by FBG2) can be estimated to ~ 40 dB and is the reason for the good efficiency of this front-end. After the second circulator (CIRC2) the signal power reaches a value of 27 mW, which will then be amplified in an 1-m long active fiber (Yb3) up to an output power of 420 mW (~ 400 mW after ISO2) when core-pumped with 650 mW by SM-LD2. The all-fiber section is closed with an 8° angle-polished end-facet and a bulk optical isolator (ISO2) to avoid back reflections. Owing to the polarizing nature of the two circulators (four transitions with a polarization extinction ratio of ~ 25 dB each) the output signal is strongly linear polarized. Usually, when using polarization-maintaining fiber-pigtailed FBG two polarization modes will propagate and cause, potentially, problems. Thus, in this case no wavelength shifted second polarization mode is observed. At this point it is worth mentioning that there exists the potential of wavelength tunability within the Yb^{3+} gain spectrum by either heating/cooling the FBG [89] or by substituting the two matched FBGs.

The output of the ASE front-end with a power of 400 mW is used as seed for the first stage, which is a polarizing 1.6-m long single-mode PCF with a 40- μ m diameter Yb-doped core region ($M_{\text{FD}} = 32 \mu\text{m}$) and a high N_{A} 200 μ m diameter inner cladding ($N_{\text{A}} \approx 0.6$). This fiber is optically pumped by a low brightness fiber-pigtailed ($\varnothing = 200 \mu\text{m}$) laser diode at 976 nm wavelength. The output beam with an obtained power of 10 W is spectrally cleaned by the use of a 4 nm bandpass interference filter (IF) to remove residual optical noise and non-signal light lying across the Yb-glass gain spectrum. The subsequent water-cooled 10.5-m long main amplifier PCF possesses an active core diameter of 42 μ m (fundamental mode $M_{\text{FD}} = 33 \mu\text{m}$) and a 500- μ m diameter core used for pumping with the 976 nm radiation from a fiber-coupled ($\varnothing = 1$ mm) laser diode. To prevent the system from lasing both fibers are prepared with angled end-facets and are optically isolated by 35 dB from each other. The measurement of output power and beam quality factor (4σ -method) versus the launched pump power has been shown in Figure 2.24a and shows again the limitation in achievable single-mode output due to mode-instabilities.

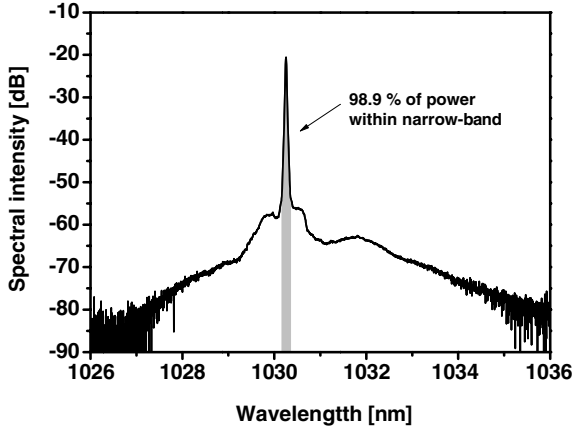


Figure 2.37 Output spectrum at maximum power of 697 W. By using an additional bandpass filter (1029–1033 nm) between the two amplifier stages non-signal light was removed before final amplification, leaving 98.9% of the power inside the 12 pm center peak.

At a maximum output power of 697 W (slope efficiency 69%) the beam quality is $M^2 = 1.34$ and an amount of 98.9% of power content has been determined in the narrow linewidth signal by a high resolution optical spectrum analyzer (Figure 2.37).

2.5.1.3 SBS Suppression Capabilities of the Narrow Linewidth ASE Source

To predict the SBS suppression capability of this system the spectral bandwidth has to be determined first. Since the spectrum is too narrow for a high-resolution grating-based optical spectrometer and too broad for most Fabry–Perot interferometers we determined the linewidth by measuring the coherence length L_c on the basis of a Michelson interferometer. With $L_c = 56$ mm and assuming a Gaussian-shaped spectrum this length corresponds to a spectral bandwidth of $\Delta\nu = 0.66 \times c_0/L_c = 3.5 \pm 0.6$ GHz ($\Delta\lambda = 12 \pm 2$ pm), with c_0 being the speed of light. The logarithmic gain G of SBS can be described by the equation (2.17), where g_B is the linear Brillouin gain coefficient, I the core intensity, and L the effective fiber length [90]:

$$G = g_B I L \left(\frac{\Delta\nu_B}{\Delta\nu_B + \Delta\nu} \right) \quad (2.17)$$

The Brillouin gain bandwidth $\Delta\nu_B$ of fused silica is ~ 30 MHz while $\Delta\nu$ of the presented ASE source is 3.5 GHz. $\Delta\nu_B$ in relation to $\Delta\nu$ (fraction in equation) shows that our ASE source has a reduced SBS gain by at least a factor of 100 (20 dB) compared to a system with a linewidth of $\leq \Delta\nu_B$. Thus, with this simple assumption 20 dB is the theoretical SBS suppression limit.

To prove this correlation experimentally, the narrow-band ASE source was compared to a single-frequency (SF) laser diode with a measured (self-heterodyne detection, 100 μ s) linewidth of 100 kHz. For this purpose the SF light was coupled in a passive 6-km long standard single mode fiber. At 4.7 mW of output power the SF light already triggers SBS, predicting the SBS threshold for the ASE source to be at

~470 mW. This value has not been reached because SRS starts to emerge at 220 mW. Nevertheless, up to this point no indication for SBS was observable. Thus, the dynamic range of this measurement only allows for proving ~17 dB of SBS suppression but the SBS threshold is expected to be even higher and, in most cases, below the SRS threshold in general. Usually, the Raman gain coefficient is 500 times (27 dB) lower than the Brillouin gain coefficient and it shows that at a certain point SBS is not the main limiting nonlinear effect anymore but rather SRS.

2.5.2

Tandem Pumping

Usually, ytterbium doped fibers are pumped at 9xx nm, for instance 915, 940, or 975 nm, where commercial high-power laser diodes are available. At the absorption maximum of Yb-doped fibers at 975 nm, the pump diodes have to be wavelength stabilized so as to not influence the fiber laser performance due to thermal wavelength drift. Furthermore, the maximum output power by this concept is either set by nonlinear optical effects, thermal, and damage issues in the amplifier itself or simply by the available pump power. The pump power for a given fiber geometry can only be increased if the brightness of the pump source is increased. To enable such high brightness pumps, the initial pump radiation from diodes can be converted by a laser process to realize an intermediate brightness enhancement (tandem pumping). Originally, the technique of tandem pumping was used to access additional wavelength of fiber lasers by generating the required pump wavelength and increased brightness by a diode pumped solid-state laser [91, 92]. Even without the requirement to access another pump wavelength, pump brightness conversion within the spectral band of ytterbium-doped double clad fibers has been demonstrated. High-power fiber lasers pumped at 915 nm have been demonstrated to emit at 976 nm with high power levels and brightness [93, 94]. The intermediate pumps for a 10 kW fiber laser, which is currently the highest available diffraction limited fiber laser, are realized by fiber lasers at 1018 nm [95]. It is necessary to use high brightness pumps to investigate the power scalability of fiber lasers in this power level range. A fiber or thin-disk laser can fulfill this brightness conversion with high efficiency. It has been suggested [96], and already shown, that a thin-disk laser at a wavelength of 1030 nm can be used as a high brightness pump source for fiber laser [97]. Further advantages have been discussed and demonstrated [98]. Tandem pumping will typically deliver a stable and power independent pump wavelength without the need for additional wavelength stabilization as in case of pump diodes. Furthermore, due to the reduced inversion level at longer pump wavelength, higher order modes and even photo-darkening might be suppressed.

In the following experiment such a tandem pumped fiber amplifier is explained in detail, where a thin-disk laser at 1030 nm is used as a high brightness pump. Two different fibers have been evaluated in high-power operation. First, a photonic crystal fiber (Figure 2.11b) is used and allows the generation of an output power of 1 kW with a slope efficiency of 73%. The second fiber, a step index large mode area (LMA) fiber, showed similar slope efficiency and an output power of 2.9 kW.

Switching the pump wavelength for an Yb-doped fiber from the peak absorption wavelength of 975 to 1030 nm reduces the pump absorption by a factor of ~ 50 – 80 . This has to be compensated for if the absorption length has to remain constant. Such compensation is possible by reducing the pump cladding diameter of the double clad fiber in order to scale Γ_p . Actually, the compensation can also be realized by increasing the doping concentration (typically leading to a higher core N_A) or by using a larger core. However, both methods usually increase the V -parameter and therefore make it difficult to achieve a reasonably good beam quality out of the fiber.

One of the advantages of using a thin disk laser as a high brightness pump is a significant increase in pump power that can be launched into the pump cladding. Considering a pump cladding diameter of $500\ \mu\text{m}$ with N_A 0.5 the available pump power from currently commercially available fiber coupled pump diodes @ 976 nm suitable for efficient coupling to the pump cladding is $\sim 7\ \text{kW}$ (from delivery fiber with $1000\ \mu\text{m}$ and N_A of 0.22). In the case of a thin disk laser one can consider a fiber with reduced pump cladding of $100\ \mu\text{m}$ (compensating reduced absorption) and an N_A of 0.2. The available pump power @ 1030 nm is $16\ \text{kW}$ (delivery fiber diameter $200\ \mu\text{m}$ and N_A of 0.10). The applicable pump power is therefore increased twofold. The photonic crystal fiber shown in Figure 2.11b is used in the experiments. It was not especially designed to work at this pump wavelength but was originally designed for short pulse amplification [99]. The pump cladding is formed by an air-cladding with an N_A of >0.5 and has a diameter of $108\ \mu\text{m}$. The laser core of $44\ \mu\text{m}$ ($\sim 33\ \mu\text{m}$ doped) with an N_A of ~ 0.03 is formed by a microstructured inner cladding. The nominal small signal pump absorption of the core material is $30\ \text{dB m}^{-1}$ for 976 nm. In comparison, the LMA fiber (from IPHT Jena) has a core of $30\ \mu\text{m}$ ($N_A \approx 0.06$) and a pump core of $100\ \mu\text{m}$ with an N_A of 0.16 obtained by a glass-glass cladding. This type of fiber has been described in detail in Reference [97], where it has been used in a similar experiment. The nominal small-signal pump absorption is $28\ \text{dB m}^{-1}$ @ 976 nm. Thus, the geometry and the optical parameters of both fibers are comparable. Figure 2.38 shows the experimental setup. The seed laser is a 400 W commercial

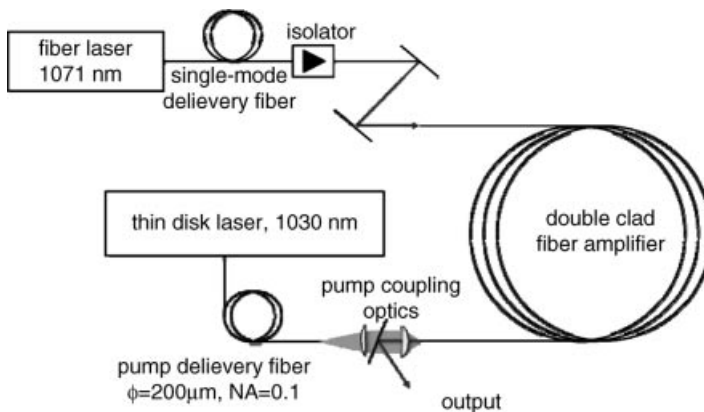


Figure 2.38 Schematic setup for the tandem pumped fiber amplifier.

monolithic fiber laser at 1071 nm with a passive delivery fiber connected to a high-power isolator for non-polarized light [100]. The coupling to the active fiber is performed free space. The pump light is delivered through a 200 μm fiber with an N_A of 0.1 by a thin disk laser and is coupled to one end of the active fiber by a 2: 1 single-lensed imaging optic designed for low focus shifting material processing. This roughly ensures the coupling to a 100 μm pump cladding. For both amplifier experiments the pump light is counter-propagating to the seed light.

To experimentally characterize the coupling efficiency at high pump power levels, a short piece of the PCF was spliced to uncoated angled endcaps (7°), which was used to avoid back reflection to the amplifier. In this experiment, the prepared fiber end at the pump side includes the endcap and a mode-stripper to strip off any undesired pump light propagating in the outer cladding of the fiber. Additionally, the endcap and the following fiber were directly water cooled. The coupling efficiency ranges between 90% and 95% for launched pump power values up to 6 kW. This indicates an almost perfect coupling to the pump cladding as it still includes losses due to Fresnel reflection at the air–glass coupling interface (two times $\sim 3.5\%$). Although the pump power of the thin-disk laser was further increased up to 11 kW (69% of the available pump power), owing to the lack of a power meter capable of measuring power levels beyond 6 kW directly, no pump coupling efficiency data are available at larger pump power. However, no experimental evidence (e.g., connector temperature, which only rose by 10 K at this power level) indicated any roll-off, so it is believed that even at these high pump-power levels a good coupling efficiency was achieved. The LMA fiber, which was used in a following experiment, was spliced to angled and anti-reflection coated endcaps to avoid Fresnel reflection. The achieved pump coupling efficiency was limited to values $>80\%$. Possible reasons might be the slightly elliptic pump cladding with a mean diameter of 102 μm and the N_A of only ~ 0.16 , which is significantly below the required minimum of 0.2 for the used coupling optic, putting stricter requirements on the alignment and tolerances.

In the first amplification experiment a PCF 18-m long was used. Both fiber endcaps and the full length of the fiber were directly water cooled. At the pump wavelength of 1030 nm the cross section for emission is larger than for absorption. To achieve sufficient amplification at the signal wavelength (1071 nm) a strong seed signal is necessary to saturate the amplifier. The remaining seed power measured after propagation through the fiber was 126 W. For all pump power levels, the unabsorbed pump light during amplification was $\sim 17\%$ (Figure 2.39). With a slope efficiency of 73% with respect to the absorbed pump power, an output power of 1 kW was extracted in this initial experiment. Figure 2.40 shows the output characteristic.

The beam quality of this fiber was measured to be $M^2 \approx 3\text{--}4$ in a different experiment using low power pump diodes at 975 nm. During the thin-disk pump experiment no M^2 measurement was performed since the near-field intensity distribution still indicated the propagation of higher order modes in the fiber core. The fiber showed irregularities, probably originating from material impurities or from the drawing process, which led to fiber failure at an optical power of 1 kW.

In the second amplifier experiment we used the LMA fiber with a length of 12 m. The seed power after the fiber was 201 W and the unabsorbed pump light was 6.4%,

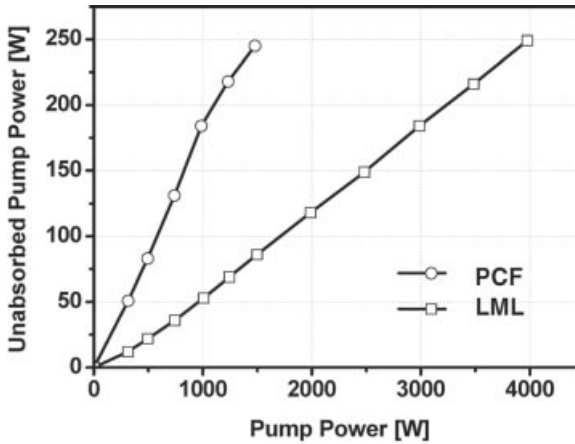


Figure 2.39 Unabsorbed pump power for both fibers used in the experiments (lines are to guide the eyes).

thus, the pump absorption was higher than for the PCF (Figure 2.39). The slope efficiency of 73% shown in Figure 2.41 with respect to the absorbed pump light is the same as for the PCF. The maximum output power of 2.9 kW was limited by unexpected damage to the endcap due to contamination of the end-face. The beam quality has been measured at the highest power level to be $M^2 \approx 5$ (4σ method – Spiricon 200 M). However, no action was taken to avoid higher order modes, that is, through tight coiling of the fiber.

Comparison of the 976 nm absorption parameters for both fibers suggests that the small-signal cladding absorption at 1030 nm should be slightly higher for the PCF than for the LMA. However, the actual cladding absorption at 1030 nm is $\sim 0.4 \text{ dB m}^{-1}$ for the PCF and $\sim 1 \text{ dB m}^{-1}$ for the LMA fiber, and was determined by

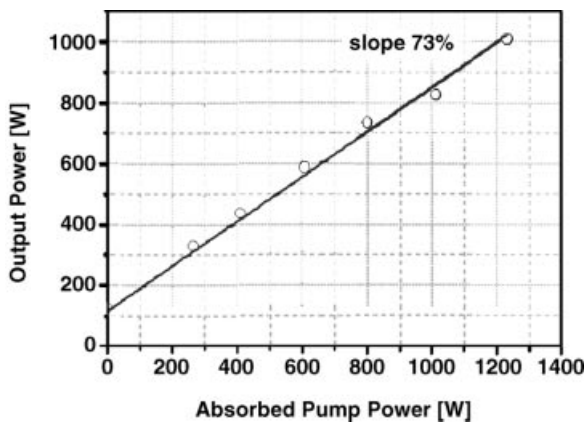


Figure 2.40 Output characteristics of the PCF amplifier fiber, with a linear fit showing a slope of 73% with respect to the absorbed pump power.

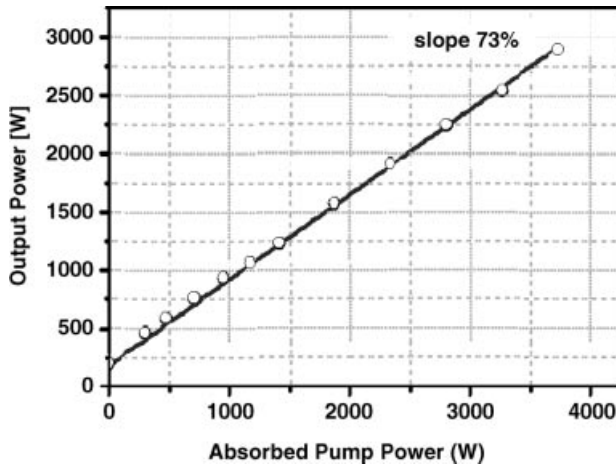


Figure 2.41 Output characteristics of the LMA fiber amplifier, with a linear fit showing a slope of 73% with respect to the absorbed pump power.

comparing the launched and the non-absorbed pump power during amplification. Since the nominal cladding absorption refers to the wavelength of 976 nm the different cladding absorption of the two fibers might be due to differing doping profiles and diverse co-dopant-concentrations used in the different manufacturing processes of the two suppliers, which affect the effective cross sections for absorption and emission at 1030 nm.

The obtained results of 1 kW of optical output power at the signal wavelength of 1071 nm from a tandem pumped photonic crystal fiber amplifier in an initial high-power experiment, and even 2.9 kW from a step-index LMA fiber, show a scalable concept for further power scaling especially when a better brightness of the pump light is required. Even though the fibers' core material was not especially designed for pumping at 1030 nm both fibers showed a good slope efficiency of 73%, which is comparable to diode pumped fibers at 976 nm.

2.5.3

Beam Combining Methods

The power scaling limitation of a single fiber laser has been basically discussed in Section 2.3 and has been theoretically studied in more detail in Reference [101]. It has been shown that single-frequency radiation can theoretically be amplified to 2 kW and even to 36 kW of diffraction-limited output power for broadband output. However, in these estimations, fiber parameters have been used that are technologically not available. For even further power scaling, different techniques for beam combining have been developed. While polarization beam-combining is limited to two orthogonal polarized beams, coherent and incoherent (spectral) combining of multiple beams offers a promising route to high-power diffraction limited laser sources.

Coherent schemes usually use the addition of multiple, phase stabilized beams in an interferometric scheme. The required phase control to achieve constructive interference is carried out by an active feedback loop [102]. Experimentally, up to 100 W combined output power has been achieved [103, 104] and recently even a power of 4 kW using eight commercial fiber amplifiers was realized [105]. In contrast, incoherent spectral beam combination (SBC) of narrow linewidth sources by wavelength selective elements has much lower requirements on the phase stability of the source and even on the spectral purity (single-frequency is not necessary), but decreases the spectral brightness. However, as a general guideline, each channel must still exhibit a narrow spectral bandwidth to preserve the good beam quality of each individual channel after a dispersive combining element due to spatial dispersion (for a detailed discussion and design criteria see References [106–108]).

Initially, SBC was successfully demonstrated using an array of laser diodes that have been imaged via a transform lens onto a grating to force them to operate at a different wavelength, where the output beam contained the spatial overlap of the individual spectral lines [109]. An array of 100 elements with an output power of 35 W has been demonstrated with this approach [110]. The technique has also been applied to fiber lasers, where the output ends of the fibers formed the array, which have been spectrally locked by the grating [111]. To increase the power, a fiber amplifier stage was added to the setup and the output was again combined by the same transform lens and the grating. This setup is shown in Figure 2.42a. With this setup 73 W of output power have been demonstrated [108].

In a different design 153 W in a diffraction limited beam has been obtained using independent seed lasers that define the spectral properties of each channel, where the amplification is based on polarized photonic crystal fiber amplifiers and highly

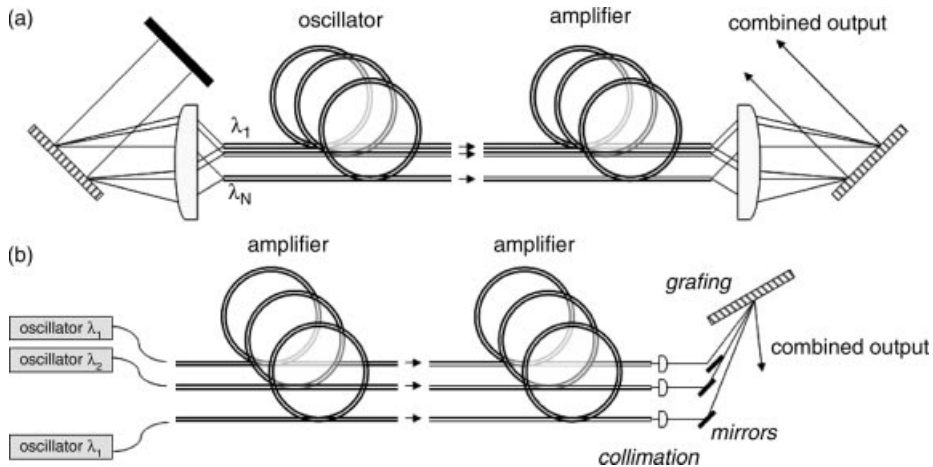


Figure 2.42 Schematic drawing of the MOPA setup using a single grating for wavelength definition in the oscillators (a) and the MOPA setup using individual narrow linewidth lasers for incoherent spectral beam combining (b).

efficient transmission grating [107]. Similarly, >500 W has been reported for different amplifier channels and the use of a holographic reflection grating [108]. Even a power of 750 W, using the narrow band reflection of volume Bragg gratings to combine the distinct channels in transmission, has been demonstrated [112]. The technique of replacing the master oscillator in Figure 2.42a by individual tunable lasers as done in these experiments, shown in Figure 2.42b, can lead to some significant advantages. Firstly, the seed lasers operate independently, thus, undesired coupling is avoided and the temporal and spectral properties can be arbitrarily chosen. Furthermore, the setup uses mirrors to achieve the spatial overlap given by the angle dispersion of the grating and therefore inherently does not use any active control. Such an experimental setup and its result are discussed in the following for continuous wave and pulsed SBC using a grating as a combining element. The geometrical aspects of the combining are given by the grating equation. For an angle close to the Littrow angle φ_{Littrow} , the angular dispersion $d\varphi_x$ in the dispersive plane x is given by:

$$d\varphi_x = \frac{1}{A} \frac{d\lambda}{\cos(\varphi_{\text{Littrow}})} \quad (2.18)$$

If $d\lambda$ corresponds to the spectral separation of two adjacent channels, $d\varphi_x$ describes the angular distance. In the following experiment, the emission wavelengths are tuned to 1040, 1048, 1056, and 1064 nm, and thus have a separation of 8 nm. The grating has a period of $A = 1040$ nm (960 lines mm^{-1}). Therefore, for the desired beam separation of ~ 3 cm in our setup the distance from the steering mirror to the grating is ~ 3 m. If $d\lambda$ corresponds to the linewidth, equation (2.18) describes the grating-induced divergence of the beam caused by its finite linewidth. Its beam quality degradation can be approximated by:

$$\Delta M_x^2 = \omega_0 \left(\frac{\pi}{2\lambda} \right) d\varphi_x \quad (2.19)$$

where $2\omega_0$ is the $1/e^2$ beam diameter on the grating.

2.5.3.1 High Average Power CW Spectral Beam Combining

Figure 2.43 shows the setup for the high average power SBC. Each amplifier chain is seeded by a low power fiber coupled wavelength tunable single-frequency ECDL that can be tuned to a specific wavelength within a wavelength range of 1010–1090 nm. The spectral linewidth has been determined by a self-heterodyne measurement to be 100 kHz. To enhance the SBS threshold in the following fiber amplifiers, the seed signal was spectrally broadened to ~ 90 pm by broadband (noise) modulation of the ECDLs pump current.

The seed signal is amplified in a first amplification stage, consisting of a core-pumped fiber amplifier to a power of ~ 500 mW. This signal is launched into the second pre-amplifier stage using a polarization-maintaining large-mode-area photonic crystal fiber. An output power of ~ 20 W in a linearly polarized and diffraction-limited beam is obtained. The ASE suppression of more than 50 dB is achieved by

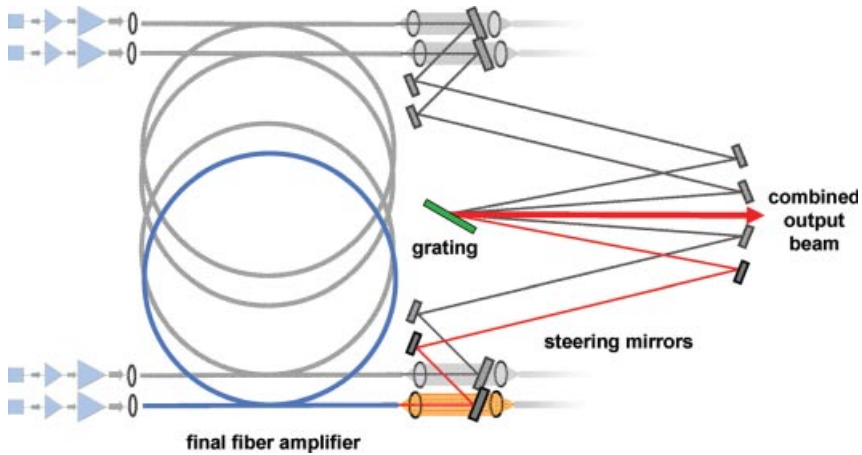


Figure 2.43 Spectral beam combining setup, including the preamplifiers, final amplifier, steering mirrors, and grating to geometrically superimpose all channels to a single output beam.

narrow-linewidth notch filters. The amplifiers are protected against back reflections and possible SBS from the main amplification stage by optical isolators. The main amplifier stage consists of a ~ 12 -m long water-cooled ytterbium-doped photonic crystal fiber prepared with endcaps and mode-strippers. The measured mode field diameter of the fundamental mode of the fiber's active core is $33\ \mu\text{m}$. The pump core is defined by an air-cladding region and has a diameter of $500\ \mu\text{m}$ and a numerical aperture of 0.5. The stage is pumped at $976\ \text{nm}$ through one fiber end-facet in counter-propagating configuration by a fiber coupled diode laser ($1\ \text{mm}$, $N_A = 0.22$). The grating, which is used as combining element, is a binary reflective diffraction grating and is optimized for highest efficiency for unpolarized light [113]. Thus, no polarization control of the main amplifier is required. In the Littrow configuration, the useful bandwidth with polarization-independent diffraction efficiency of $>95\%$ is experimentally measured in the range 1010 – $1090\ \text{nm}$.

Each amplifier can generate a stable output power of $\sim 2.1\ \text{kW}$, limited by the available pump power with a typical slope efficiency of 70% . The slope of output power versus pump power is linear due to the wavelength stabilized pump diodes at $976\ \text{nm}$. The beam quality stays close to diffraction limited of $M^2 < 1.5$ up to a power of $\sim 600\ \text{W}$. However, the beam quality out of the fiber is decreased with further increased power (typical value: $M^2 \approx 2.0$ @ $750\ \text{W}$, $M^2 \approx 3.5$ @ $2.1\ \text{kW}$) due to mode-instabilities. Owing to this onset of higher order transversal modes and the reduced corresponding intensity within the fiber core, the SBS threshold for fundamental mode operation could not be determined. However, with the linewidth of $\sim 90\ \text{pm}$ no significant power in the backward direction was observed up to a power level of $2.1\ \text{kW}$. Since the grating is polarization independent no means of polarization control were introduced and especially above the onset of higher order modes the beam has no defined state of polarization and appears to be non-polarized.

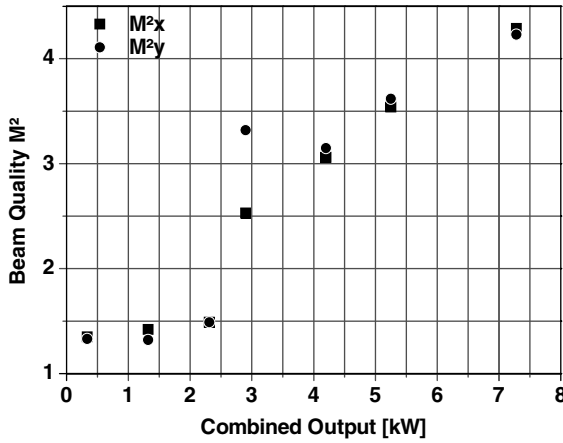


Figure 2.44 Beam quality measured after the combining grating with respect to the output power. Beam quality degradation caused by mode-instability in the individual fiber amplifiers can be observed above 2.5 kW.

The four channels were geometrically overlapped in near and far field by two steering mirrors and the collimation lens after the fiber. Only minor beam quality degradation is observed with proper alignment and is mainly given by residual misalignment as well as by the finite spectral width of 90 pm causing additional divergence in the dispersive plane of the grating. The beam diameter on the grating was $2\omega_0 = 3$ mm and the calculated beam quality degradation according to equation (2.19) is approximately $\Delta M_x \approx 0.2$. Figure 2.44 shows the beam quality with respect to the combined output power after the grating, up to a power level of 7.3 kW. The beam quality of $M^2 \leq 1.5$ up to a power level of 2.3 kW proves good alignment to ensure the required near- and far-field overlap. The threshold-like beam quality degradation above the combined power of 2.3 kW corresponds to the already mentioned mode-instability in the individual channel at ~ 600 W.

Figure 2.45 shows the power of the combined beam with respect to the total pump power. It includes the combining efficiency of the grating and shows a slope efficiency of 68%. The combining efficiency for all four channels is $\sim 99\%$ independent of the output power and was determined by the power in the 0th diffraction order with the assumption that scattering losses at the grating are negligible. A direct measurement of the ratio of incident and diffracted light at a low power level verified this result. Owing to the large time constants of high-power thermal sensors as power meters, a direct measurement of such a low loss was not possible at high power levels. The ASE background can be estimated to be below 1% based on the spectra measured directly after the amplifier (>55 dB peak suppression). No experimental evidence of scattering losses is given. Figure 2.46 shows the combined beams spectrum with a wavelength separation of 8 nm. In the experiment a combined output power of 8.2 kW could be obtained. The beam quality has been conserved with respect to the individual channels.

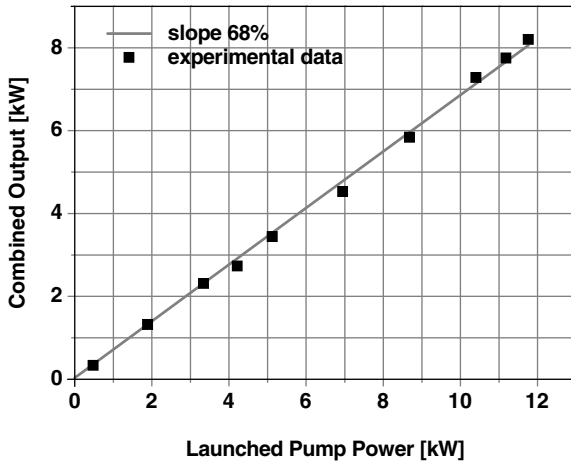


Figure 2.45 Optical power of the combined beam with respect to the total pump power.

2.5.3.2 Pulsed SBC

The technique described for CW spectral beam combining also offers the possibility of scaling the power and energy for pulsed sources beyond the limitations of a single amplifier. Similarly to the effects described in Section 2.3, the generation of intense pulses is limited due to the high peak intensities sustained over long propagation lengths. In the case of nanosecond fiber amplifiers, effects are related not only to nonlinear refraction, such as four-wave mixing and self-phase-modulation, but also stimulated Raman and Brillouin scattering cause instabilities and loss of spectral purity. State-of-the-art fiber amplifiers using advanced PCF can produce and sustain megawatts of peak power and several millijoule pulse energy [114, 115].

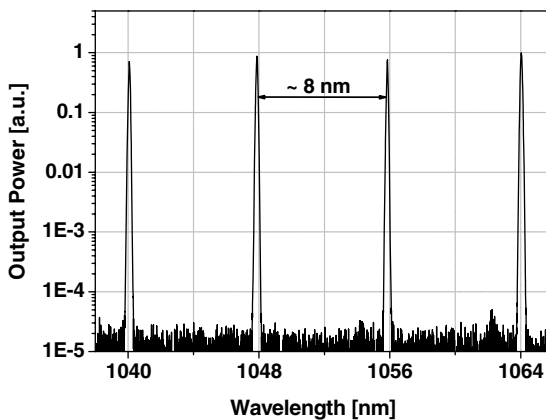


Figure 2.46 Spectral composition of the combined beam measured with an OSA at 20 pm resolution.

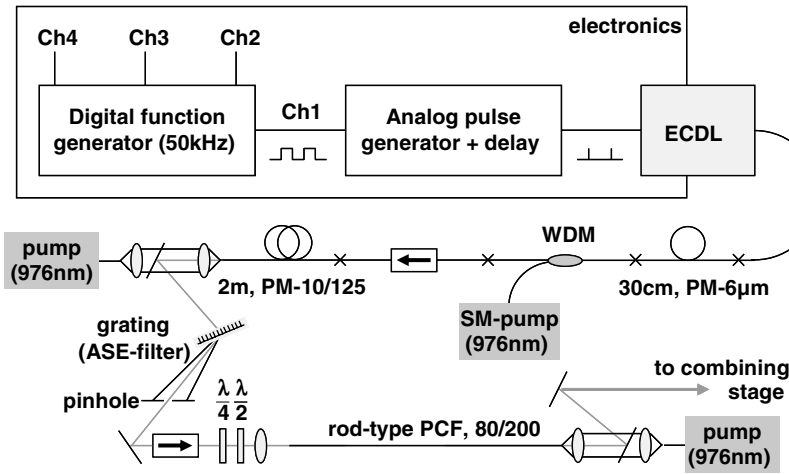


Figure 2.47 Experimental setup of a single fiber amplifier chain used in the pulsed beam combining setup.

The fundamental limitation regarding pulse peak power is determined by self-focusing, which cannot be compensated by larger mode-field diameters [116]. Experimentally, a pulse peak power of 4.5 MW in a 1 ns-pulsed fiber amplifier setup has been demonstrated [117].

The setup defined in Figure 2.43 has been modified to include a temporal-delay control of the individual pulsed sources as shown in Figure 2.47. This is done by electronically triggering the four individual seed lasers with such a delay that the combined beams overlap temporally by compensating the different optical path in each channel. In detail, Figure 2.47 shows one of the four employed three-stage amplifier systems that run at slightly different wavelengths between 1030 and 1036 nm (separation ~ 2 nm) and emit 2 ns pulses with a narrow emission bandwidth of ~ 75 pm (FWHM).

The rather weak optical signal (~ 5 μ W average power, 50 kHz repetition rate) is pre-amplified up to 100 mW in a two-stage monolithic polarization-maintaining ytterbium-doped fiber amplifier system consisting of a 30-cm long core-pumped 6/125 μ m and a 2-m long cladding pumped 10/125 μ m PM-fiber. To filter the ASE produced in these amplifiers, a grating is used as a narrowband ASE filter before seeding the main amplifier fiber, which is a 1.2-m long rod-type ytterbium-doped photonic crystal fiber with a ytterbium-doped 80 μ m active core and a pump core of 200 μ m ($N_A \sim 0.58$). Owing to the large core, the fiber offers guidance for a few transverse modes. Stable fundamental mode operation can be achieved by proper seed signal mode matching. The amplified beams are highly polarized (degree of polarization = 95%) and directed to the 1.8-m long combining stage (distance folding mirror-grating) similar to the one used in the CW experiments. The combining grating has a larger period of 1740 lines mm^{-1} , which was optimized for TE polarization at Littrow illumination, resulting in a diffraction efficiency of $>97\%$.

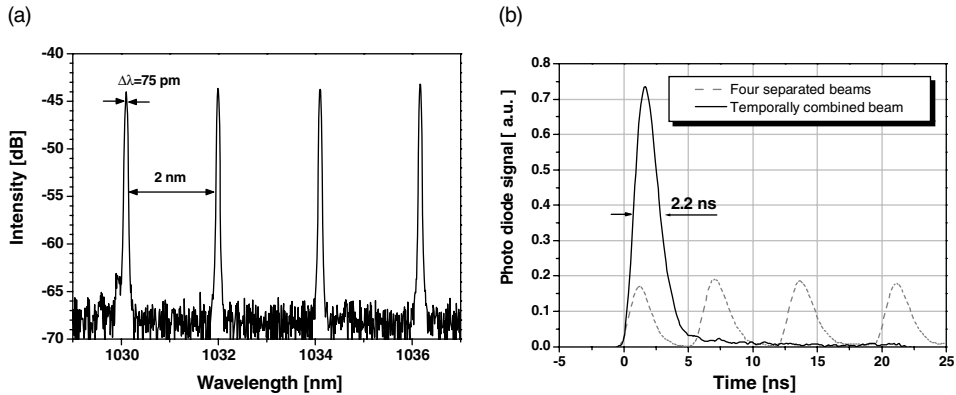


Figure 2.48 Temporal overlap (a) and spectrum of the output beam after combination at 187 W, 3.7 mJ (b).

in a wavelength range from 1020 to 1070 nm. In the relevant spectral range 1030–1036 nm a diffraction efficiency of $>99\%$ for linear polarized light has been measured, which makes this type of gratings an ideal low loss all-reflective combining element in this case.

For a well-determined angle of incidence and a spectral separation of 2 nm (Figure 2.48a) the four beams are diffracted into one single combined beam with a measured M^2 of 1.3 in the vertical and 2.3 in the horizontal direction (4σ method, SpiriconTM). It should be mentioned that the beam quality degradation in horizontal direction depends critically on the pulse duration. As an example, at a pulse duration of 10 ns the seed lasers emit a spectral bandwidth of 40 pm, resulting in a horizontal M^2 of 1.7. This is in accordance with the calculated beam degradation of Equation 2.19.

The temporal overlap correction is carried out by the electronic delay as shown in Figure 2.48b, resulting in a combined pulse duration of 2.2 ns, which is equivalent to a single emission. Therefore, no significant timing-jitter induced pulse broadening was observed. The combined average output power was as high as 187 W with an efficiency of $>97\%$ due to the high efficiency of the grating and high degree of polarization of the output beams. At this power level and a repetition rate of 50 kHz a pulse energy of $>3.7 \text{ mJ}$ was achieved, resulting in a pulse peak power of 1.7 MW. It should be emphasized that these results are not fundamentally limited and with a revised more powerful version of the preamplifier stage, the current saturation of the main amplifiers can be shifted to much higher output power levels to a similar level of the CW experiments discussed before.

Both experiments, for CW and pulsed sources, prove the potential of SBC. The useful Yb-gain bandwidth covers more than 50 around 1060 nm. Together with the demonstrated separation of 2 nm, the SBC setup would allow the combination of many more channels, hence, a scaling beyond 100 kW for CW and 100 mJ for pulsed beam appears to be feasible in a straightforward manner.

2.6

Summary

High-power fiber lasers have attracted much attention in recent years. The basic design guidelines for the fibers used in these systems as well as special fibers have been presented in Section 2.2. The understanding of core design presented there is the requirement for the scaling of nonlinear effects that typically limit the output parameters of fiber lasers. The fundamentals regarding nonlinear effects are given in Section 2.3. In addition, the rate equations and thermo-optical effects have been discussed in the most basic forms. Another limitation not yet fully understood is mode-instabilities, which have also been introduced in this chapter. From a more practical point of view, some handling aspects in terms of fiber preparation such as endcaps preparation, mode strippers, and the pump coupling schemes are highlighted in Section 2.4. All these fundamentals can be found in the description of the high-power experiments described in Section 2.5. Nevertheless, the presentation given here is far from complete. Further important developments can be found in subsequent chapters of this book. In addition, the high average power and especially high peak power scaling of ultrashort fiber laser systems [118] will benefit from further advances in the field of fiber manufacturing as well as the theoretical understanding of these complex systems pushed to their upper limits.

References

- 1 Kapron, F.P., Keck, D.B., and Maurer, R.D. (1970) Radiation losses in glass optical waveguides. *Appl. Phys. Lett.*, **17**, 423.
- 2 Snitzer, E. (1961) Cylindrical dielectric waveguide modes. *J. Opt. Soc. Am.*, **51**, 491–498.
- 3 Snitzer, E. (1961) Optical maser action of Nd^{3+} in a barium crown glass. *Phys. Rev. Lett.*, **7**, 444–446.
- 4 Koester, C.J. and Snitzer, E. (1964) Amplification in a fiber laser. *Appl. Opt.*, **3**, 1182–1186.
- 5 Hayashi, I., Panish, M.B., Foy, P.W., and Sumski, S. (1970) Junction lasers which operate continuously at room temperature. *Appl. Phys. Lett.*, **17**, 109–111.
- 6 Mears, R.J., Reekie, L., Jauncey, I.M., and Payne, D.N. (1987) Low-noise erbium-doped fibre amplifier at 1.54 μm . *Electron. Lett.*, **23**, 1026–1028.
- 7 Tünnermann, A., Schreiber, T., Röser, F., Liem, A., Höfer, S., Zellmer, H., Nolte, S., and Limpert, J. (2005) The renaissance and bright future of fibre lasers. *J. Phys. B: At. Mol. Opt. Phys.*, **38**, 681.
- 8 Bedö, S., Lüthy, W., and Weber, H.P. (1993) The effective absorption coefficient in double-clad fibres. *Opt. Commun.*, **99** (5–6), 331–335.
- 9 Agrawal, G.P. (2008) *Applications of Nonlinear Fiber Optics (Optics and Photonics Series)*, Academic Press.
- 10 Kirchhof, J., Unger, S., Schwuchow, A., Jetschke, S., and Knappe, B. (2005) Dopant interactions in high power laser fibers, in *Optical Components and Materials II* (ed. S. Jiang and M.J. Digonnet), Proceedings of SPIE, vol. 5723, SPIE, pp. 261–272.
- 11 Unger, S., Schwuchow, A., Dellith, J., and Kirchhof, J. (2007) Codoped materials for high power fiber lasers – diffusion behaviour and optical properties, in *Optical Components and Materials IV* (ed. S. Jiang and M.J. Digonnet), Proceedings of SPIE, vol. 6469, SPIE, pp. 646913.

- 12 Riishede, J., Niels, A.M., and Laegsgaard, J. (2003) A 'poor man's approach' to modelling micro-structured optical fibers. *J. Opt. A: Pure Appl. Opt.*, **5**, 534–538.
- 13 Gloge, D. (1971) Weakly guiding fibers. *Appl. Opt.*, **10**, 2252–2258.
- 14 Marcuse, D. (1977) Loss analysis of single-mode fiber splices. *Bell Syst. Tech. J.*, **56**, 703.
- 15 Fermann, M.E. (1998) Single-mode excitation of multimode fibers with ultrashort pulses. *Opt. Lett.*, **23** (1), 52–54.
- 16 Marcuse, D. (1982) Influence of curvature on the losses of doubly clad fibers. *Appl. Opt.*, **21** (23), 4208–4213.
- 17 Koplow, J.P., Kliner, D.A.V., and Goldberg, L. (2000) Single-mode operation of a coiled multimode fiber amplifier. *Opt. Lett.*, **25** (7), 442–444.
- 18 Liu, C., Chang, G., Litchinitser, N., Guertin, D., Jacobsen, N., Tankala, K., and Galvanauskas, A. (2007) Chirally coupled core fibers at 1550-nm and 1064-nm for effectively single-mode core size scaling. Presented at Conference on Lasers and Electro-Optics/Quantum Electronics and Laser Science Conference and Photonic Applications Systems, paper CTuBB3, Optical Society of America.
- 19 Donlagic, D. (2006) In-line higher order mode filters based on long highly uniform fiber tapers. *J. Lightwave Technol.*, **24** (9), 3532–3539.
- 20 Bhutta, T., Mackenzie, J.I., Shepherd, D.P., and Beach, R.J. (2002) Spatial dopant profiles for transverse-mode selection in multimode waveguides. *J. Opt. Soc. Am. B*, **19** (7), 1539–1543.
- 21 Siegman, A.E. (2007) Gain-guided, index-antiguidded fiber lasers. *J. Opt. Soc. Am. B*, **24** (8), 1677–1682.
- 22 Eidam, T., Rothhardt, J., Stutzki, F., Jansen, F., Hädrich, S., Carstens, H., Jauregui, C., Limpert, J., and Tünnermann, A. (2011) Fiber chirped-pulse amplification system emitting 3.8 GW peak power. *Opt. Express*, **19** (1), 255–260.
- 23 Limpert, J., Schmidt, O., Rothhardt, J., Röser, F., Schreiber, T., Tünnermann, A., Ermeneux, S., Yvernault, P., and Salin, F. (2006) Extended single-mode photonic crystal fiber lasers. *Opt. Express*, **14** (7), 2715–2720.
- 24 Stutzki, F., Jansen, F., Eidam, T., Steinmetz, A., Jauregui, C., Limpert, J., and Tünnermann, A. (2011) High average power large-pitch fiber amplifier with robust single-mode operation. *Opt. Lett.*, **36** (5), 689–691.
- 25 Bjarklev, Anders, Broeng, Jes, and Sanchez Bjarklev, Araceli, (2003) *Photonic Crystal Fibres*, 1st edn, Springer.
- 26 Saitoh, K. and Koshiba, M. (2005) Empirical relations for simple design of photonic crystal fibers. *Opt. Express*, **13**, 267–274.
- 27 Saitoh, K., Tsuchida, Y., Koshiba, M., and Niels, A.M. (2005) Endlessly single-mode holey fibers: the influence of core design. *Opt. Express*, **13**, 10833–10839.
- 28 Knight, J., Birks, T., Russell, P., and Atkin, D. (1996) All-silica single-mode optical fiber with photonic crystal cladding. *Opt. Lett.*, **21**, 1547.
- 29 Birks, T., Knight, J., and Russell, P. (1997) Endlessly single-mode photonic crystal fiber. *Opt. Lett.*, **22**, 961–963.
- 30 Uranus, H.P. (2010) Theoretical study on the multimodeness of a commercial endlessly single-mode PCF. *Opt. Commun.*, **283** (23), 4649–4654.
- 31 Russell, P. (2003) Photonic crystal fibers. *Science*, **299** (5605), 358–362.
- 32 Dong, L., Peng, X., and Li, J. (2007) Leakage channel optical fibers with large effective area. *J. Opt. Soc. Am. B*, **24** (8), 1689–1697.
- 33 Jansen, F., Stutzki, F., Otto, H.-J., Baumgartl, M., Jauregui, C., Limpert, J., and Tünnermann, A. (2010) The influence of index-depressions in core-pumped Yb-doped large pitch fibers. *Opt. Express*, **18** (26), 26834–26842.
- 34 Stutzki, F., Jansen, F., Eidam, T., Steinmetz, A., Jauregui, C., Limpert, J., and Tünnermann, A. (2011) High average power large-pitch fiber amplifier with robust single-mode operation. *Opt. Lett.*, **36**, 689–691.
- 35 Stutzki, Fabian, Jansen, Florian, Jauregui, Cesar, Limpert, Jens, and

- Tünnermann, Andreas (2011) Non-hexagonal large-pitch fibers for enhanced mode discrimination. *Opt. Express*, **19**, 12081–12086.
- 36 Jansen, Florian, Stutzki, Fabian, Jauregui, Cesar, Limpert, Jens, and Tünnermann, Andreas (2011) Avoided crossings in photonic crystal fibers. *Opt. Express*, **19**, 13578–13589.
 - 37 Issa, N.A. (2004) High numerical aperture in multimode microstructured optical fibers. *Appl. Opt.*, **43**, 6191–6197.
 - 38 Bouwmans, G., Percival, R.M., Wadsworth, W.J., Knight, J.C., and Russell, P.St.J. (2003) High-power Er:Yb fiber laser with very high numerical aperture pump-cladding waveguide. *Appl. Phys. Lett.*, **83**, 817–818.
 - 39 Ortigosa-Blanch, A., Knight, J.C., Wadsworth, W.J., Arriaga, J., Mangan, B.J., Birks, T.A., and Russell, P.S.J. (2000) Highly birefringent photonic crystal fibers. *Opt. Lett.*, **25**, 1325–1327.
 - 40 Hansen, T.P., Broeng, J., Libori, S.E.B., Knudsen, E., Bjarklev, A., Jensen, J.R., and Simonsen, H. (2001) Highly birefringent index-guiding photonic crystal fibers. *IEE Photon. Technol. Lett.*, **13**, 588–590.
 - 41 Folkenberg, J.R., Nielsen, M.D., Mortensen, N.A., Jakobsen, C., and Simonsen, H.R. (2004) Polarization maintaining large mode area photonic crystal fiber. *Opt. Express*, **12**, 956–960.
 - 42 Folkenberg, J.R., Nielsen, M.D., and Jakobsen, C. (2005) Broadband single-polarization photonic crystal fiber. *Opt. Lett.*, **30**, 1446–1448.
 - 43 Schmidt, O., Rothhardt, J., Eidam, T., Röser, F., Limpert, J., Tünnermann, A., Hansen, K.P., Jakobsen, C., and Broeng, J. (2008) Single-polarization ultra-large-mode-area Yb-doped photonic crystal fiber. *Opt. Express*, **16**, 3918–3923.
 - 44 Giles, C.R. and Desurvire, E. (1991) Modeling erbium-doped fiber amplifiers. *J. Lightwave Technol.*, **9** (2), 271–283.
 - 45 Paschotta, R., Nilsson, J., Tropper, A.C., and Hanna, D.C. (1997) Ytterbium-doped fiber amplifiers. *IEEE J. Quantum Electron.*, **33** (7), 1049.
 - 46 Brown, D. and Hoffman, H.J. (2001) Thermal, stress, and thermo-optic effects in high average power double-clad silica fiber lasers. *IEEE J. Sel. Top. Quantum Electron.*, **2**, 207–217.
 - 47 Krause, W. (1986) *Gerätekonstruktion*, Verlag Technik, Berlin.
 - 48 Zintzen, B., Langer, T., Geiger, J., Hoffmann, D., and Loosen, P. (2007) Heat transport in solid and air-clad fibers for high-power fiber lasers. *Opt. Express*, **15**, 16787–16793.
 - 49 Limpert, J., Schreiber, T., Liem, A., Nolte, S., Zellmer, H., Peschel, T., Guyenot, V., and Tünnermann, A. (2003) Thermo-optical properties of air-clad photonic crystal fiber lasers in high power operation. *Opt. Express*, **11**, 2982–2990.
 - 50 Hädrich, S., Schreiber, T., Pertsch, T., Limpert, J., Peschel, T., Eberhardt, R., and Tünnermann, A. (2006) Thermo-optical behavior of rare-earth-doped low-NA fibers in high power operation. *Opt. Express*, **14**, 6091–6097.
 - 51 Smith, R.G. (1972) Optical power handling capacity of low loss optical fibers as determined by stimulated Raman and Brillouin scattering. *Appl. Opt.*, **11**, 2489–2494.
 - 52 Jauregui, Cesar, Limpert, Jens, and Tünnermann, Andreas (2009) Derivation of Raman threshold formulas for CW double-clad fiber amplifiers. *Opt. Express*, **17**, 8476–8490.
 - 53 Hasegawa, A. and Brinkman, W.F. (1980) Tunable coherent IR and FIR sources utilizing modulational instability. *IEEE J. Quantum Electron.*, **16**, 694–697.
 - 54 Tai, K., Hasegawa, A., and Tomita, A. (1986) Observation of modulational instability in optical fibers. *Phys. Rev. Lett.*, **56**, 135–138.
 - 55 Agrawal, G.P. (1987) Modulational instability induced by cross-phase modulation. *Phys. Rev. Lett.*, **59**, 880–883.
 - 56 Liao, S., Gong, M., and Zhang, H. (2009) Theoretical calculation of beam quality factor of large-mode-area fiber amplifiers. *Laser Phys.*, **19** (3), 437–444.
 - 57 Schmidt, O., Rekas, M., Wirth, C., Rothhardt, J., Rhein, S., Kliner, A., Strecker, M., Schreiber, T., Limpert, J., Eberhardt, R., and Tünnermann, A. (2011) High power narrow-band

- fiber-based ASE source. *Opt. Express*, **19**, 4421–4427.
- 58 Eidam, T., Hanf, S., Seise, E., Andersen, T.V., Gabler, T., Wirth, C., Schreiber, T., Limpert, J., and Tünnermann, A. (2010) Femtosecond fiber CPA system emitting 830W average output power. *Opt. Lett.*, **35**, 94–96.
 - 59 Wirth, C., Schreiber, T., Rekas, M., Tsybin, I., Peschel, T., Eberhardt, R., and Tünnermann, A. (2010) High-power linear-polarized narrow linewidth photonic crystal fiber amplifier, in *Fiber Lasers VII: Technology, Systems and Applications* (ed. K. Tankala), Proceedings of SPIE, vol. 7580, SPIE, p. 75801.
 - 60 Jiang, Z. and Marcianti, J.R. (2008) Impact of transverse spatial-hole burning on beam quality in large-mode-area Yb-doped fibers. *J. Opt. Soc. Am. B*, **25**, 247–254.
 - 61 Jauregui, C., Eidam, T., Limpert, J., and Tünnermann, A. (2011) The impact of modal interference on the beam quality of high-power fiber amplifiers. *Opt. Express*, **19**, 3258–3271.
 - 62 Andermahr, N. and Fallnich, C. (2010) Optically induced long-period fiber gratings for guided mode conversion in few-mode fibers. *Opt. Express*, **18**, 4411–4416.
 - 63 Frisken, S.J. (1992) Transient Bragg reflection gratings in erbium-doped fiber amplifiers. *Opt. Lett.*, **17**, 1776–1778.
 - 64 Dignonnet, M.J.F., Sadowski, R.W., Shaw, H.J., and Pantell, R.H. (1997) Resonantly enhanced nonlinearity in doped fibers for low-power all-optical switching: a review. *Opt. Fiber Technol.*, **3** (1), 44–64.
 - 65 Smith, Arlee V. and Smith, Jesse J. (2011) Mode instability in high power fiber amplifiers. *Opt. Express*, **19**, 10180–10192.
 - 66 Andrew, D. (2005) *Yablon: Optical Fiber Fusion Splicing*, Springer-Verlag, Berlin.
 - 67 Boehme, S., Beckert, E., Eberhardt, R., and Tuennermann, A. (2009) Laser splicing of end caps: process requirements in high power laser applications, in *Laser-Based Micro- and Nanopackaging and Assembly III* (eds W. Pfleging, Y. Lu, K. Washio, W. Hoving, and J. Amako), Proceedings of SPIE, vol. 7202, SPIE, p. 720205.
 - 68 Limpert, J., Röser, F., Klingebiel, S., Schreiber, T., Wirth, C., Peschel, T., Eberhardt, R., and Tünnermann, A. (2007) The rising power of fiber lasers and amplifiers. *IEEE J. Sel. Top. Quantum Electron.*, **13** (3), 537–545.
 - 69 Tünnermann, A., Limpert, J., and Nolte, S. (2007) Industrial perspectives of ultrafast fiber lasers. CLEO/Europe and IQEC 2007 Conference Digest, (Optical Society of America, 2007), paper TF1_1.
 - 70 Gapontsev, V.P. (2008) Penetration of fiber lasers into industrial market. Presented at Fiber Lasers V: Technology, Systems, and Applications, Photonics West, San Jose 2008, paper 6873-01.
 - 71 Ancona, A., Döring, S., Jauregui, C., Röser, F., Limpert, J., Nolte, S., and Tünnermann, A. (2009) Femtosecond and picosecond laser drilling of metals at high repetition rates and average powers. *Opt. Lett.*, **34**, 3304–3306.
 - 72 Rippin, D.J. and Goldberg, L. (1995) High efficiency side-coupling of light into optical fibres using imbedded v-grooves. *Electron. Lett.*, **31**, 2204–2205.
 - 73 Koplow, J.P., Moore, S.W., and Kliner, D.A.V. (2003) A new method for side pumping of double clad fiber sources. *J. Quant. Electron.*, **39**, 529–540.
 - 74 Xu, J., Lu, J., Kumar, G., Lu, J., and Ueda, K. (2003) A non-fused fiber coupler for side-pumping of double-clad fiber lasers. *Opt. Commun.*, **220**, 389–395.
 - 75 Cesar Jauregui, Steffen Böhme, Georgios Wenetiadis, Jens Limpert, and Andreas Tünnermann, (2010) “All-fiber side pump combiner for high-power fiber lasers and amplifiers”, in *Fiber Lasers VII: Technology, Systems, and Applications* (eds K. Tankala), Proceedings of SPIE, vol. 7580, page 75801E.
 - 76 Gonthier, F. (2008) Method and device for optically coupling optical fibers, International Patent Application WO, 2008/083482.
 - 77 Digiovanni, D.J. and Stentz, A.J. (1999) Tapered fiber bundles for coupling light and out of cladding-pumped fiber devices, US patent, 5,864,644.

- 78 Gonthier, F., Martineau, L., Seguin, F., Villeneuve, A., Faucher, M., Azami, N., and Garneau, M. (2006) Optical coupler comprising multimode fibers and method of making the same, US patent 7,046,875.
- 79 Mathieu Faucher, Eric Villeneuve, Benoit Sevigny, Alexandre Wetter, Roger Perreault, Yannick Keith Lizé, and Nigel Holehouse, (2008) "High power monolithically integrated all-fiber laser design using single-chip multimode pumps for high reliability operation", in *Fiber Lasers V: Technology, Systems, and Applications* (eds J. Broeng, C. Headley III), Proceedings of SPIE, vol. 6873, page 68731T.
- 80 Gapontsev, V. and Samartsev, I. (1999) Coupling arrangement between a multi-mode light source and an optical fiber through an intermediate optical fiber length, US patent 5,999,673.
- 81 Albinsson, N.L.J., Kevan, D.M., William, T.P., Borisovich, G.A., Morten, I., Nickolaos, Z.M., and Neil, P.D. (2007) Multi-fibre arrangement for high power fibre lasers and amplifiers, US Patent No. 7,221,822.
- 82 Nikolajsen, T. (2007) Optical coupler device, methods of their production and use, Patent Application WO/2007/006317.
- 83 Kim, J.K., Hagemann, C., Schreiber, T., Peschel, T., Böhme, S., Eberhardt, R., and Tünnermann, A. (2010) Monolithic all-glass pump combiner scheme for high-power fiber laser systems. *Opt. Express*, **18**, 13194–13203.
- 84 Mermelstein, M.D. (2009) SBS threshold measurements and acoustic beam propagation modeling in guiding and anti-guiding single mode optical fibers. *Opt. Express*, **17**, 16225–16237.
- 85 Kobayakov, A., Sauer, M., and Chowdhury, D. (2010) Stimulated Brillouin scattering in optical fibers. *Adv. Opt. Photon.*, **2**, 1–59.
- 86 Noda, J., Okamoto, K., and Sasaki, Y., (1986) "Polarization-maintaining fibers and their applications," *Lightwave Technology, Journal of*, vol. 4, no. 8, 1071–1089.
- 87 Jackson, S.D. (2002) Direct evidence for laser re-absorption as initial cause for self-pulsing in three-level fiber lasers. *Electron. Lett.*, **38**, 1640–1642.
- 88 Upadhyaya, B.N., Kuruvilla, A., Chakravarty, U., Shenoy, M.R., Thyagarajan, K., and Oak, S.M. (2010) Effect of laser linewidth and fiber length on self-pulsing dynamics and output stabilization of single-mode Yb-doped double-clad fiber laser. *Appl. Opt.*, **49**, 2316–2325.
- 89 Rothhardt, J., Hädrich, S., Gottschall, T., Limpert, J., Tünnermann, A., Rothhardt, M., Becker, M., Brückner, S., and Bartelt, H. (2009) Generation of flattop pump pulses for OPCPA by coherent pulse stacking with fiber Bragg gratings. *Opt. Express*, **17**, 16332–16341.
- 90 Herráez, M.G., Song, K.Y., and Thévenaz, L. (2006) Arbitrary-bandwidth Brillouin slow light in optical fibers. *Opt. Express*, **14**, 1395–1400.
- 91 Grubb, S.G., Humer, W.F., Cannon, R.S., Windhorn, T.H., Vendetta, S.W., Sweeney, K.L., Leilabady, P.A., Barnes, W.L., Jedrzejewski, K.P., and Townsend, J.E. (1992) + 21 dBm erbium power amplifier pumped by a diode-pumped Nd:YAG laser. *IEEE Photonics Technol. Lett.*, **4** (6), 553–555.
- 92 Minelly, J.D., Jedrzejewski, K.P., Taylor, E.R., Wang, Ji, Payne, D.N., Raven, A.L., Mannonen, I., Fernie, D.P., and Hayden, J.S. (1994) High-power diode-pumped Nd³⁺ fiber laser, in *Biomedical Fiber Optic Instrumentation* (eds J.A. Harrington, D.M. Harris, and A. Katzir) Proceedings of SPIE, vol. 2131, SPPIE, pp. 292–300.
- 93 Röser, F., Jauregui, C., Limpert, J., and Tünnermann, A. (2008) 94W 980nm high brightness Yb-doped fiber laser. *Opt. Express*, **16** (22), 17310–17318.
- 94 Boulet, J., Zaouter, Y., Desmarchelier, R., Cazaux, M., Salin, F., Saby, J., Bello-Doua, R., and Cormier, E. (2008) High power ytterbium-doped rod-type three-level photonic crystal fiber laser. *Opt. Express*, **16**, 17891–17902.
- 95 Fomin, V., Abramov, M., Ferin, A., Abramov, A., Mochalov, D.,

- Platonov, N., and Gapontsev, V. (2010) 10kW single mode fiber laser. SyTu-1.3, presented at Symposium on High-Power Fiber Lasers, 14th International Conference "Laser Optics 2010", St. Petersburg.
- 96 Kumkar, M. and Voss, A. (2005) High-power fiber laser amplifier and fiber laser oscillator, Patent WO/2005/122345.
- 97 A. Popp, A. Voss, Th. Graf, S. Unger, J. Kirchhof, and H. Bartelt, (2010) "Thin-disk-laser-pumped ytterbium-doped fiber laser with an output power in the kW range", in *Solid State Lasers and Amplifiers IV, and High-Power Lasers* (eds T. Graf, J. I. Mackenzie, H. Jelinková, G. G. Paulus, V. Bagnoud, C. Le Blanc), Proceedings of SPIE, vol. 7721, page 772102.
- 98 Codemard, C.A., Sahu, J.K., and Nilsson, J. (2010) Tandem cladding-pumping for control of excess gain in ytterbium-doped fiber amplifiers. *IEEE J. Quantum Electron.*, **46** (12), 1860–1869.
- 99 Limpert, J., Schmidt, O., Rothhardt, J., Röser, F., Schreiber, T., Tünnermann, A., Ermeneux, S., Yvernault, P., and Salin, F. (2006) Extended single-mode photonic crystal fiber lasers. *Opt. Express*, **14**, 2715–2720.
- 100 Nicklaus, K. and Langer, T. (2010) Faraday isolators for high average power fundamental mode radiation, in *Solid State Lasers XIX: Technology and Devices* (eds W.A. Clarkson, N. Hodgson, and R.K. Shori), Proceedings of SPIE, vol. 7578, SPIE, pp. 75781U–75781U-10.
- 101 Dawson, J.W., Messerly, M.J., Beach, R.J., Shverdin, M.Y., Stappaerts, E.A., Sridharan, A.K., Pax, P.H., Heebner, J.E., Siders, C.W., and Barty, C.P.J. (2008) Analysis of the scalability of diffraction-limited fiber lasers and amplifiers to high average power. *Opt. Express*, **16**, 13240–13266.
- 102 Fan, T.Y. (2005) Laser beam combining for high power, high-radiance sources. *IEEE J. Quantum Electron.*, **11**, 567–577.
- 103 Loftus, T.H., Thomas, A.M., Norsen, M., Minelly, J., Jones, P., Honea, E., Shakir, S.A., Hendow, S., Culver, W., Nelson, B., and Fitelson, M., Four-channel, high power, passively phase locked fiber array. Presented at Advanced Solid-State Photonics (ASSP) 2008, OSA Technical Digest Series (CD) (Optical Society of America, 2008), paper WA4, on CD ROM.
- 104 Wickham, M., Cheung, E.C. Ho, J.G., Goodno, G.D. Rice, R.R., Rothenberg, J. Thielen, P., and Weber, M., Coherent combination of fiber lasers with a diffractive optical element. Presented at Advanced Solid-State Photonics 2008, OSA Technical Digest Series (CD) (Optical Society of America, 2008), paper WA5, on CD ROM.
- 105 Yu, C.X., Augst, S.J. Redmond, S.M., Goldizen, K.C. Murphy, D.V., Sanchez, A., and Fan, T.Y. (2011) Coherent combining of a 4kW, eight-element fiber amplifier array. *Opt. Lett.*, **36**, 2686–2688.
- 106 Augst, S.J., Ranka, J.K. Fan, T.Y., and Sanchez, A. (2007) Beam combining of ytterbium fiber amplifiers (invited). *J. Opt. Soc. Am. B*, **24**, 1707–1715.
- 107 Klingebiel, S., Röser, F. Ortaç, B., Limpert, J., and Tünnermann, A. (2007) Spectral beam combining of Yb-doped fiber lasers with high efficiency. *J. Opt. Soc. Am. B*, **24**, 1716–1720.
- 108 Loftus, T.H., Thomas, A.M. Hoffman, P.R., Norsen, M. Royse, R., Liu, A., and Honea, E.C. (2007) Spectrally beam-combined fiber lasers for high-average-power applications. *IEEE J. Sel. Top. Quantum Electron.*, **13**, 487–497.
- 109 Daneu, V., Sanchez, A., Fan, T.Y., Choi, H.K., Turner, G.W., and Cook, C.C. (2000) Spectral beam combining of a broad-stripe diode laser array in an external cavity. *Opt. Lett.*, **25**, 405–407.
- 110 Chann, B., Huang, R.K., Missaggia, L.J., Harris, C.T., Liau, Z.L., Goyal, A.K., Donnelly, J.P., Fan, T.Y., Sanchez-Rubio, A., and Turner, G.W. (2005) Near-diffraction-limited diode laser arrays by wavelength beam combining. *Opt. Lett.*, **30**, 2104–2106.
- 111 Augst, S.J., Goyal, A.K., Aggarwal, R.L., Fan, T.Y., and Sanchez, A. (2003) Wavelength beam combining of ytterbium fiber lasers. *Opt. Lett.*, **28**, 331–333.

- 112 Sevan, A., Andrusyak, O., Ciapurin, I., Smirnov, V., Venus, G., and Glebov, L. (2008) Efficient power scaling of laser radiation by spectral beam combining. *Opt. Lett.*, **33**, 384–386.
- 113 Clausnitzer, T., Limpert, J., Zöllner, K., Zellmer, H., Fuchs, H., Kley, E., Tünnermann, A., Jupé, M., and Ristau, D. (2003) Highly efficient transmission gratings in fused silica for chirped-pulse amplification systems. *Appl. Opt.*, **42**, 6934–6938.
- 114 Schmidt, O., Rothhardt, J., Röser, F., Linke, S., Schreiber, T., Rademaker, K., Limpert, J., Tünnermann, A., Ermenoux, S., Yvernault, P., and Salin, F. (2007) Millijoule pulse energy Q-switched short-length fiber laser. *Opt. Lett.*, **31**, 1551–1553.
- 115 Brooks, C.D. and Di Teodoro, F. (2006) Multimegawatt peak-power, single-transverse-mode operation of a 100- μm core diameter, Yb-doped rodlike photonic crystal fiber amplifier. *Appl. Phys. Lett.*, **89** (11), 111119–111122.
- 116 Farrow, R.L., Hadley, G.R., Smith, A.V., and Kliner, D.A.V. (2007) Numerical modeling of self-focusing beams in fiber amplifiers, in *Fiber Lasers IV: Technology, Systems, and Applications* (eds D.J. Harter, A. Tünnermann, J. Broeng, and C. HeadleyIII), Proceedings of SPIE, **6453**, SPIE, p, 645309.
- 117 Cheng, M.-Y., Chang, Y.-C., Galvanauskas, A., Mamidipudi, P., Changkakoti, R., and Gatchell, P. (2005) High-energy and high-peak-power nanosecond pulse generation with beam quality control in 200- μm core highly multimode Yb-doped fiber amplifiers. *Opt. Lett.*, **30**, 358–360.
- 118 Limpert, J., Röser, F., Schimpf, D.N., Seise, E., Eidam, T., Hadrich, S., Rothhardt, J., Misas, C.J., and Tünnermann, A. (2009) High repetition rate gigawatt peak power fiber laser-systems: Challenges, design, and experiment. *IEEE JSTQE*, **15** (1), 159.